Ideal Scan Path for High-Speed Atomic Force Microscopy

Dominik Ziegler, Travis R. Meyer, Andreas Amrein, Andrea L. Bertozzi, and Paul D. Ashby

***Abstract*—We propose a new scan waveform ideally suited for high-speed atomic force microscopy. It is an optimization of the Archimedean spiral scan path with respect to the *X,Y* scanner bandwidth and scan speed. The resulting waveform uses a constant angular velocity spiral in the center and transitions to constant linear velocity toward the periphery of the scan. We compare it with other scan paths and demonstrate that our novel spiral best satisfies the requirements of high-speed atomic force microscopy by utilizing the scan time most efficiently with excellent data density and data distribution. For accurate *X,Y*, and *Z* positioning our proposed scan pattern has low angular frequency and low linear velocities that respect the instruments mechanical limits. Using sensor inpainting we show artifact-free high-resolution images taken at two frames per second with a 2.2 μm scan size on a moderately large scanner capable of 40 μm scans.**

Q1

***Index Terms*—Actuators, atomic force microscopy (AFM), motion control.**

I. Introduction

ATOMIC force microscopy (AFM) techniques acquire high-resolution images by scanning a sharp tip over a sample while measuring the interaction between the tip and sample [1]. AFM has the ability to image material surfaces with exquisite resolution [2]. Furthermore, careful probe design facilitates nanoscale measurement of specific physical or chemical properties, such as surface energy [3], [4] or electrostatic [5], [6] and magnetic [7], [8] forces. Therefore, AFM has become one of the most frequently used characterization tools in nanoscience. However, the sequential nature of scanning limits the speed of data acquisition and most instruments take several minutes to obtain a high-quality image. The productivity and use of AFM would increase dramatically if the speed could match the imaging speeds of other scanning microscopes, such as confocal and scanning electron microscopes [9]. The semiconductor industry, which requires detection of nanoscopic defects over large areas, is an important driver for higher scan speeds [10]. More importantly, higher temporal resolution enables the exploration of dynamic chemical and biomolecular processes [11]. This is especially important for dynamic nanoscale phenomena of materials that are sensitive to the radiation associated with light and electron microscopy making AFM the best characterization tool.

Significant engineering effort over the last decade has pushed the speed limits of AFM to a few frames per second [12]–[15]. Most researchers operate within the raster scan paradigm, where the tip is moved in a zig-zag pattern over the sample at a constant speed in the image area. The rationale for the raster pattern is that with regular sampling and constant scanner velocity image rendering is simple because the data points align with the pixels of the image spatially. However, achieving accurate images is challenging because piezoelectric nanopositioners have notoriously nonlinear displacement response and the mechanical resonances of the high-inertia scanner amplify the harmonics of the waveform that are required to create the turnaround region of the raster scan. Working within the raster scan paradigm, most methods to speed up the AFM have focused on the mechanical design. The most common means to build fast scanners is to reduce the size of the scanner and increase stiffness [16]–[22] so that the scanner actuates effectively at higher frequencies but this places strict limitations on the mass of the sample.

Using nonraster scan waveforms with low-frequency components provides an opportunity to increase imaging speed. Lissajous scans have been shown to be advantageous for high-speed scanning because they can cover the entire scan area using a sinusoidal scan pattern of constant amplitude and frequency [23], [24]. Similarly, cycloid [25] and spirograph [26] scans use a single frequency circular scan with a constant offset between adjacent loops.

In this paper, we analyze the suitability of spiral scan paths for high-speed scanning. Having constant distance between loops makes Archimedean spirals especially useful. They can be performed either using constant angular velocity (CAV) [27]–[30] or constant linear velocity (CLV) [31], [32]. At least a twofold increase in temporal or spatial resolution is achieved over raster scanning because, when generating an image, almost 100% of the data is used instead of throwing away trace or retrace data. Furthermore, spiral scan patterns require less bandwidth and

Manuscript received March 3, 2016; revised July 2, 2016; accepted August 21, 2016. Recommended by Technical Editor G. Cherubini. This work was supported in part by the National Science Foundation under Grant DMS-1118971, in part by the Office of Naval Research under Grant N000141210838, in part by the Small Business Innovation Research Phase I and II Grants under Award DE-SC 0013212, and in part by the National Science Foundation under Award 1556128. The work at Molecular Foundry was supported by the Office of Science, Office of Basic Energy Sciences, U.S. Department of Energy under Contract DE-AC02-05CH11231.

D. Ziegler is with the Molecular Foundry, Lawrence Berkeley National Laboratory, Berkeley, CA 94720 USA, and also with the Scuba Probe Technologies LLC, Alameda, CA 94501 USA (e-mail: dziegler@lbl.gov).

A. Amrein and P. D. Ashby are with the Molecular Foundry, Lawrence Berkeley National Laboratory, Berkeley, CA 94720 USA (e-mail: andi.amrein@gmail.com; pdashby@lbl.gov).

T. R. Meyer and A. L. Bertozzi are with the Department of Mathematics, University of California Los Angeles, Los Angeles, CA 90095 USA (e-mail: euphopiab@gmail.com; bertozzi@math.ucla.edu).

Color versions of one or more of the figures in this paper are available online at http://ieeexplore.ieee.org.

Digital Object Identifier 10.1109/TMECH.2016.2615327

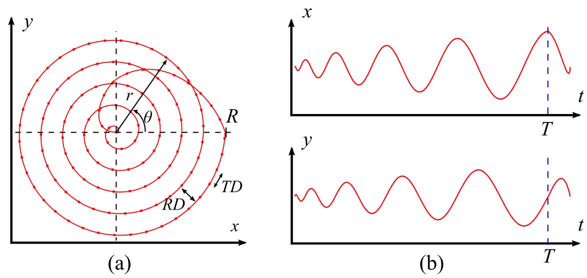

Fig. 1. (a) Illustration of an Archimedean spiral showing outward and truncated inward scan paths to quickly return to the starting point at the origin. For clarity only a small number of loops of $N = 5$ is used in the outward spiral. The radial and tangential sampling distances are specified by RD and TD, respectively. (b) Transforming r and θ into Cartesian coordinates gives the *X* and *Y* motion of the piezo. The vertical dotted line at time T marks the transition from outward scan to the truncated inward scan.

are better suited to drive high-inertia nanopositioners for fast scanning. However, most of today's nonraster scan attempts use sensors to steer the probe over the sample using a closed-loop configuration. This slows down the achievable frame rates. We have shown that ultimate control over the position is not required for accurate imaging. When sensors detect the position, an accurate image can be reconstructed using inpainting algorithms [33]–[36] from data recorded along any arbitrary open-loop path. The technique, which we call sensor inpainting [37], frees AFM from the paradigm of raster scanning and the need for slower closed-loop control of scanner position. We have used sensor inpainting to render images from Archimedean spiral and spirograph scan patterns [26], [37].

In this paper, we analyze Archimedean spiral scan patterns for their suitability for fast scanning. We propose a new Archimedean spiral, which we call the optimal spiral, that combines the benefits of CAV and CLV scans. The proposed spiral scan follows an Archimedean scan path but respects the mechanical limits of the instrument by balancing velocity and angular frequency to obtain the optimum data distribution for accurate high-speed scanning when scan velocity needs to be minimized.

II. Description of Scan Path

A. Tip Velocity and Angular Velocity

Fig. 1(a) shows an example of Archimedean spiral with five loops for the outward path and a fast inward path to return to the starting point at the origin. We describe the outward scan pattern using polar coordinates $r(t)$ and $\theta(t)$ as functions of the scan time. The time required to complete the outward scan is T and t_* is the dimensionless quantity $t_* = t/T$

$$r = Rf(t_*) \tag{1}$$

$$\theta = 2\pi N f(t_*) \tag{2}$$

where N is the number of loops and R is the desired radius. To fully scan the circular area, it is required that $f(0) = 0$ and $f(1) = 1$, but in principle $f(t_*)$ can be of any arbitrary shape. When eliminating the temporal function one obtains the polar expression of an Archimedean spiral in the form of

$$r(\theta) = \frac{R\theta}{2\pi N}. \tag{3}$$

In an Archimedean spiral, the scan radius r increases by a constant pitch R/N for each full revolution, and the maximal scan radius R is reached exactly after N full loops. Experimentally, the scan pattern applied to the piezo is achieved by transforming r and θ into Cartesian coordinates [see Fig. 1(b)].

The tip velocity v_s and angular velocity $\dot{\theta}$ are given by

$$v_s(r,\theta) = \sqrt{(r\dot{\theta})^2 + \dot{r}^2} \tag{4}$$

$$v_s(t_*) = \frac{Rf'(t_*)}{T}\sqrt{(2\pi N f(t_*))^2 + 1} \tag{5}$$

$$\dot{\theta}(t_*) = \frac{2\pi N}{T} f'(t_*). \tag{6}$$

We denote the derivative with respect to time t with a dot and the derivative with respect to t_* with a prime.

B. Data Density and Data Distribution

The Archimedean spirals analyzed here have different functions for $f(t_*)$ such that they follow the same scan path, but with different tip velocities. As a consequence, different data point distributions result when using a constant sampling frequency F_s. Fig. 1(a) shows the sampling along the spiral path and the radial distance (RD) and tangential distance (TD) between data points. The general expressions for radial distance (RD) and tangential distance (TD) are given by

$$\mathrm{RD}(r,\theta) = \frac{2\pi\dot{r}}{\dot{\theta}}, \quad \mathrm{TD}(r,\theta) = \frac{r\dot{\theta}}{F_s}. \tag{7}$$

The local data density δ is expressed by the inverse of the product of TD and RD and represents the samples per unit area as

$$\delta(r) = \frac{1}{\mathrm{TD}\cdot\mathrm{RD}} = \frac{F_s}{2\pi r\dot{r}} \tag{8}$$

$$\delta(t_*) = \frac{n}{2\pi R^2 f(t_*) f'(t_*)} \tag{9}$$

where n is the number of samples, $n = F_s T$. Having uniform density throughout the image is ideal for maximizing the information being measured from the sample. Furthermore, it is important to have good homogeneity η of the sample density, i.e., an even distribution of the data points in all directions. The ratio of RD to TD describes such homogeneity by comparing the spacing between data points

$$\eta(r,\theta) = \frac{\mathrm{RD}}{\mathrm{TD}} = \frac{2\pi F_s \dot{r}}{(\dot{\theta})^2 r} \tag{10}$$

$$\eta(t_*) = \frac{n}{2\pi N^2 f(t_*) f'(t_*)}. \tag{11}$$

As discussed in earlier work [37] when using isotropic inpainting algorithms such as heat equation, $\eta = 1$ results in the best rendering with least artifacts.

By definition Archimedean spirals have constant RD, and the density δ and homogeneity η simplify to

$$\delta(r,\theta) = \frac{NF_s}{Rr\dot{\theta}}, \quad \eta(r,\theta) = \frac{F_s R}{Nr\dot{\theta}}. \tag{12}$$

III. CLV Spiral

An Archimedean spiral with essentially constant velocity along the scan path is the result of $f(t_*)=\sqrt{t_*}$ [see Fig. 2(a)]. For this case, the tip velocity is given by

$$v_{s_{\mathrm{CLV}}}(t_*) = \frac{R\sqrt{(2\pi N)^2 t_* + 1}}{2T\sqrt{t_*}} \approx \frac{\pi N R}{T}. \tag{13}$$

Toward the very center of the image $v_{s_{\mathrm{CLV}}}$ theoretically approaches infinity. In discrete implementations, however, the velocity decreases [see Fig. 2(a)] because the high frequencies for small r in the position signal are lost due to the spacing of samples. When $t_* \gg 1/(2\pi N)^2$ the velocity rapidly approaches a constant. Similarly, toward the very center of the image, the angular frequency function goes to infinity

$$\dot{\theta}(t_*)_{\mathrm{CLV}} = \frac{\pi N}{T\sqrt{t_*}} \tag{14}$$

except for the discrete implementation. To maintain CLV angular frequency more than two orders of magnitudes higher in the center than on the periphery of the image is required [see Fig. 2(b)]. Note that the area under the velocity curve [see Fig. 2(a)] represents the total arc length ($\approx$0.3 mm), while the area under the angular frequency curve [see Fig. 2(b)] corresponds to the number of loops $N = 85$. These values remain constant for all spiral scans described here.

The expressions for density δ_{CLV} and η_{CLV} are independent of time t_* and radius r and simplify to

$$\delta_{\mathrm{CLV}} \approx \frac{n}{\pi R^2} \tag{15}$$

$$\eta_{\mathrm{CLV}} \approx \frac{n}{\pi N^2}. \tag{16}$$

We imaged a sample of copper evaporated onto annealed gold because the contrast in size between the copper and gold grains creates high information content. This makes this sample an ideal image to test the accuracy of the data collection and rendering when scanning quickly. The sample has complex features of different sizes and the smallest feature resolvable by the tip is $\approx$25 nm. We used a Cypher ES by Oxford Instruments equipped with a piezoelectric scanner having 40 μm range in X and Y, 4 μm range in Z, and low-noise position sensors. While using a contact mode in constant height mode we used a sampling frequency F_s of 50 kHz to impose limited bandwidth on the data collection as if we were operating with force feedback and were limited by the z-feedback loop and tip–sample interaction. This makes the data and analysis most relevant to the majority of AFM performed in constant force mode. The scan is 2.2 μm in size with $N = 85$ loops and collected in 0.5 s producing a scan velocity of 600 mm/s. Using the Nyquist criterion for information content, the $\approx$25 nm feature size, and 50 kHz sampling frequency, we calculate that $v_s \approx$625 mm/s should be the scan speed limit for accurate imaging. Constant δ and η, resulting from theoretical constant velocity v_s and sampling F_s produces an ideal dataset with $n = 25$ k data points. In the density map, Fig. 2(c), the color represents the number of recorded data points that fall within each pixel. All collected deflection data points are inpainted within a circular image with a diameter of 256 pixels containing about 50k pixels. The insets are magnifications of the center (A), middle (B), and periphery (C) of the scan showing that the data density is the same throughout

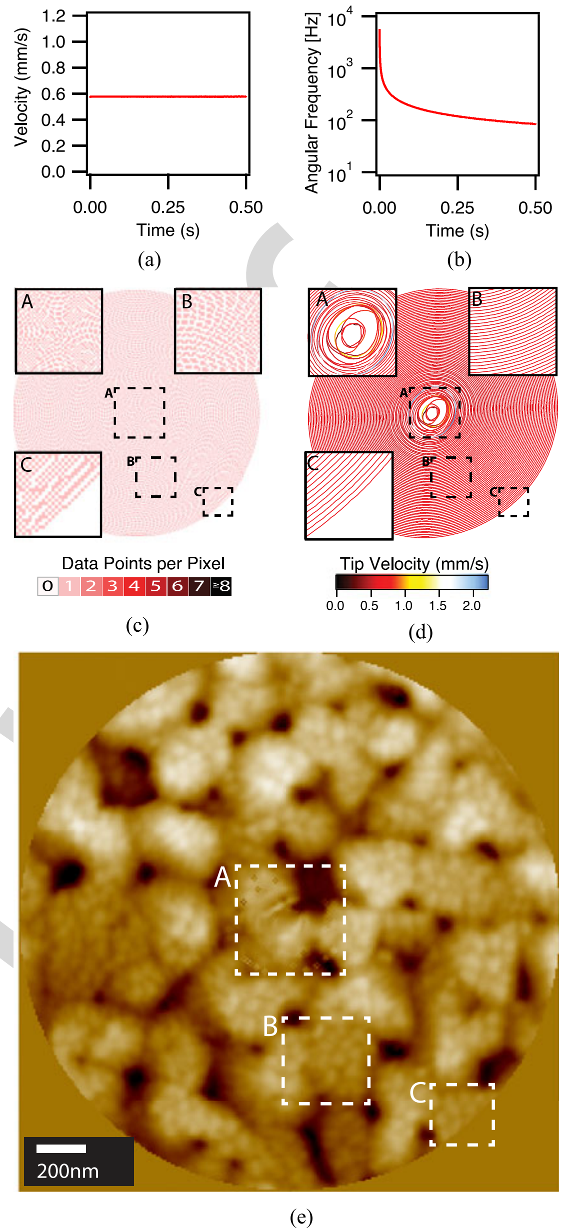

Fig. 2. CLV spiral. (a) Velocity as a function of scan time is constant. (b) To maintain constant speed at small radii the angular frequency “blows up” to values exceeding the resonance frequency of the scanner. (c) Theoretical spatial data density distribution showing number of samples per pixel in the rendered image. (d) Scan path, as measured with the sensors, during the CLV spiral scan. Color scale represents velocity of the scanner. (e) A CLV image of copper evaporated onto annealed gold. The relatively slow scan speed and excellent sample density at the outer edge of the image lead to good fidelity of the features. The features in the boxes (A, B, C) are compared with other scan waveforms in Fig. 5.

the scan. At most each pixel contains one data point. The insets show the great homogeneity of the data distribution resulting for CLV scans.

The scan path measured by the sensors on the scanner is shown in Fig. 2(d) and it is slightly oblong from lower left to upper right. The high angular frequencies used in the center of the scan exceed 8 kHz and excite the resonance of the scanner. This increases the radius causing poor sampling in the center of the scan and erratic motion as evidenced by the very fast motion of greater than 2 mm/s [see Fig. 2(d) inset A]. The CLV spiral scan of the copper/gold sample is shown in Fig. 2(e). We used sensor inpainting [37] to create a 2.0 μm round image, 256 pixels wide, which trimmed the data and used ≈20 kS such that there are ≈ 0.25 data points per pixel. The CLV scan captures the features of the sample very well except in the center where there is obvious distortion and artifacts from driving at very high angular frequency. Therefore, in order to prevent distortions in the image, the angular velocity is required to match the bandwidth of the scanner.

IV. CAV Spiral

CAV scans drive the piezos at a single frequency. This helps to prevent the above-mentioned distortions due to the resonances of the scanner. CAV scans use the simplest linear function

$$f(t_*) = t_* \tag{17}$$

where the resulting angular velocity, Fig. 3(b), is simply given by the number of revolutions in the total time

$$\dot{\theta}(t_*)_{\mathrm{CAV}} = \frac{2\pi N}{T}. \tag{18}$$

The velocity $v_{s_{\mathrm{CAV}}}$ increases nearly linearly with time for CAV spirals as the radius increases. The function for scan velocity

$$v_{s_{\mathrm{CAV}}}(t_*) = \frac{R}{T}\sqrt{4(\pi N t_*)^2 + 1} \approx \frac{2\pi N R}{T} t_* \tag{19}$$

simplifies to a linear function of t_*, for almost all of the scan, as shown in Fig. 3(a).

Using (1), (8), (10), and (17) the expressions for data density δ and homogeneity η simplify to the following radial dependencies:

$$\delta(r)_{\mathrm{CAV}} \approx \frac{n}{2\pi R r} \tag{20}$$

$$\eta(r)_{\mathrm{CAV}} \approx \frac{nR}{2\pi N^2 r}. \tag{21}$$

Data density for a CAV spiral scan with similar scan parameters as those used for Fig. 2 is shown in Fig. 3(c). Because the scan velocity is near zero at the center of the image the data density is extremely high reaching 74 samples in the center pixels. Conversely the data density δ becomes sparse toward the periphery. Since the scan time T and number of loops N are the same as the CLV scan [see Fig. 2(c)], the average value of η is also one but the value drops to 0.5 at the periphery where features start to be undersampled. We imaged the copper/gold sample in the same location as Fig. 2(e) using a CAV spiral. The measured scan path, Fig. 3(d), has very even spacing radially because the scanner responds with constant mechanical gain and phase lag when driven at constant angular frequency. The measured velocity matches the theoretical values well. The inpainted image is shown in Fig. 3(e). The features in the center of the image are reproduced well due to the slow angular frequency, high sampling, and η but the periphery is under sampled and the features become blurred.

The need to capture the information at the periphery of the image determines the sampling rate and velocity for CAV spirals. Therefore, for most of the scan, near the center, the instrument is going too slow and wasting precious time. Neither CLV nor CAV spirals are ideal for imaging the sample quickly but each

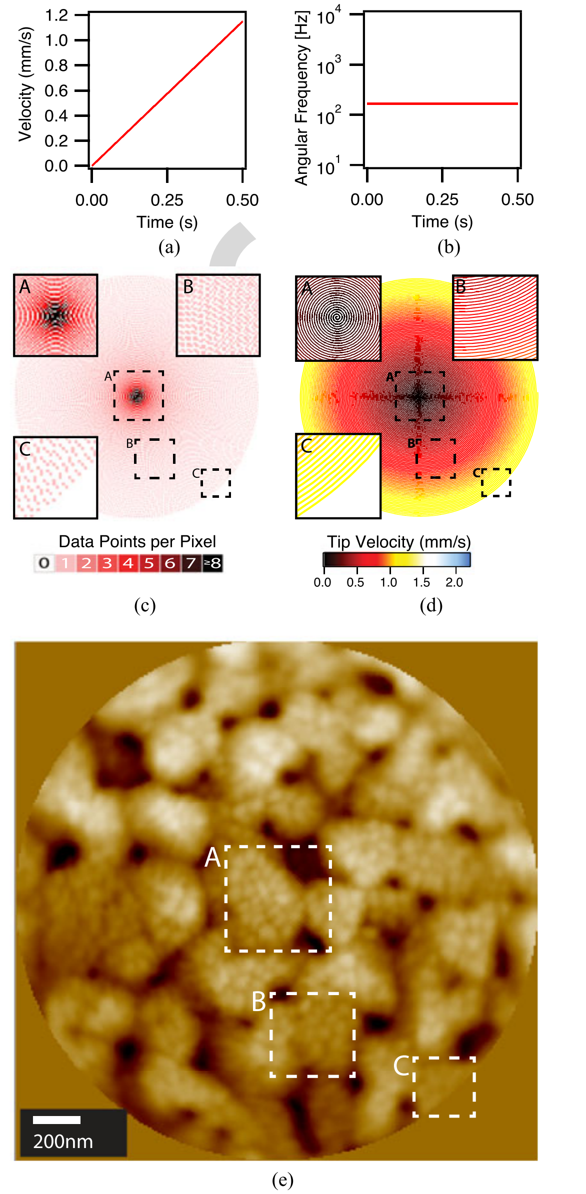

Fig. 3. CAV spiral. (a) Velocity as a function of scan time increases linearly and (b) angular frequency is constant. (c) Theoretical data density is very high in the center and getting sparse toward the periphery. (d) The velocity is low in the middle and high on the periphery. (e) CAV image of copper evaporated onto annealed gold at same location as Fig. 2. The CAV eliminates errors in the center of the image but the high linear velocity and sparse data at the edges smears out features. The features in the boxes are compared with other scan waveforms in Fig. 5.

has properties that are advantageous. The optimal Archimedean spiral combines the advantages of both.

V. Optimal Archimedean Spiral (OPT)

The ideal Archimedean spiral would have the shortest scan times while respecting the instrument's mechanical limits. The time function $f(t_*)$ of the Archimedean spiral can be any arbitrary shape leading to various scan speeds and frequencies. As observed in Fig. 2, the mechanical gain of the resonance can lead to large excursions from the intended scan path and inaccuracies. It is best if the *X*,*Y* scan frequencies stay well below the resonance. Similarly, high tip speeds lead to sparse data, Fig. 3, or high tip–sample forces from poor *Z*-piezo feedback making tip speed an equally important optimization parameter.

We solved for the optimal time function $f(t_*)$ using maximum *X*,*Y* scan frequency ω_L and tip speed v_L as limiting criteria. The complete optimization is found in Appendix 1 and has similarities with the optimization method of Tuma *et al.* [38]. The resulting waveform follows ω_L in the center of the scan and then follows v_L at the periphery. Effectively, the waveform combines the benefits of CAV and CLV scans. We call the new scan waveform the optimal Archimedean spiral (OPT).

The optimal Archimedean spiral is the fastest Archimedean spiral that respects the limits of *X*,*Y* scanner bandwidth and scan speed. In our experience, the parameter of scan time and scan speed are equally valid independent variables for the parameterization of the OPT so we also present a parameterization that follows the optimal principle of performing CAV in the center and CLV at the periphery but uses scan time as an independent variable.

The CLV is produced when $f(t_*) = \sqrt{t_*}$ and the CAV is produced when $f(t_*) = t_*$ with t_* dimensionless time. Let the angular frequency limit of the AFM be given by $\frac{d\theta}{dt} \leq \omega_L$. Define $a \equiv \frac{2\pi N}{T\omega_L}$. To push the angular frequency limit initially the composite spiral's f must be of the form $f(t_*) = \frac{t_*}{a}$ as this results in $\frac{d\theta}{dt} = \omega_L$. Using the CAV up to sometime t_{*L} then transitioning to a CLV spiral with parameters C_1 and C_2 means the optimum Archimedean spiral has a function f of the form

$$f(t_*) = \begin{cases} \frac{t_*}{a} & \text{if } t_* \leq t_{*L} \\ \sqrt{C_1 t_* + C_2} & \text{if } t_* > t_{*L}. \end{cases} \tag{22}$$

To find the parameters, t_{*L}, C_1, and C_2, we enforce three properties of the final spiral. The scan should be finished at time $t_* = 1$ hence $f(1) = 1$ and f and f' should be continuous at t_{*L}.

The three conditions imply, in order, the equations

$$1 = \sqrt{C_1 + C_2} \tag{23}$$

$$\frac{t_{*L}}{a} = \sqrt{C_1 t_{*L} + C_2} \tag{24}$$

$$\frac{1}{a} = \frac{C_1}{2}(C_1 t_{*L} + C_2)^{-\frac{1}{2}}. \tag{25}$$

The first equation implies $C_2 = 1 - C_1$ and substituting (24) into (25) yields

$$\frac{1}{a} = \frac{C_1 a}{2t_{*L}}. \tag{26}$$

Therefore,

$$C_1 = \frac{2t_{*L}}{a^2} \tag{27}$$

$$C_2 = 1 - \frac{2t_{*L}}{a^2} \tag{28}$$

which after substituting into (24) produces a quadratic equation in t_{*L}:

$$0 = t_{*L}^2 - 2t_{*L} + a^2 \tag{29}$$

$$\Rightarrow t_{*L} = 1 \pm \sqrt{1 - a^2}. \tag{30}$$

The discriminant is positive provided $a < 1$, which is violated only when the scan cannot be completed in the given time subject to the given angular frequency limit. As the transition must take place in the scan time $t_{*L} \in [0, 1]$ the negative sign is the natural solution hence

$$t_{*L} = 1 - \sqrt{1 - a^2} \tag{31}$$

is the transition time t_{*L}.

According to (5), the speed of the tip for this f at time t_{*L} is

$$v(t_{*L}) = \frac{R}{aT}\sqrt{1 + \left(\frac{2\pi N}{a}\right)^2 t_{*L}^2} \approx \frac{\pi N R}{T}\frac{2t_{*L}}{a^2}. \tag{32}$$

The velocity curve for an optimal Archimedean spiral scan is shown in Fig. 4(a). The velocity increases linearly and quickly because the angular frequency is at the limit. When the normalized time t_* reaches t_{*L} the scan transitions to CLV with constant velocity and decreasing angular frequency, as shown in Fig. 4(b). The density image, shown in Fig. 4(c), is mostly homogeneous throughout. At the center, inset A, the data density is high because of the short section of CAV spiral but otherwise samples are evenly spread over the whole image, insets B and C, where η is very close to one. We again imaged the copper/gold sample in the same location as Fig. 2(e) but using an OPT spiral of the same time, number of loops, and sampling rate. Like the CAV spiral, the scan path is evenly spaced throughout the image but the velocity is always low, as shown in Fig. 4(d). The features throughout the image are reproduced well showing the superior performance of the OPT, as shown in Fig. 4(e).

VI. Discussion

A. Further Criteria for Comparing Waveforms

Increasing the frame rate of scanning probe techniques is essential for capturing dynamic processes at the nanoscale. Here we introduce design criteria that allow further comparison of various scan waveforms to determine the best scan wave for fast scanning. As we already mentioned in the optimization to create the OPT waveform, the scan must respect the mechanical bandwidth of the *X*,*Y* scanner, i.e., the scan waveform needs to have sufficiently low angular frequency to avoid positioning

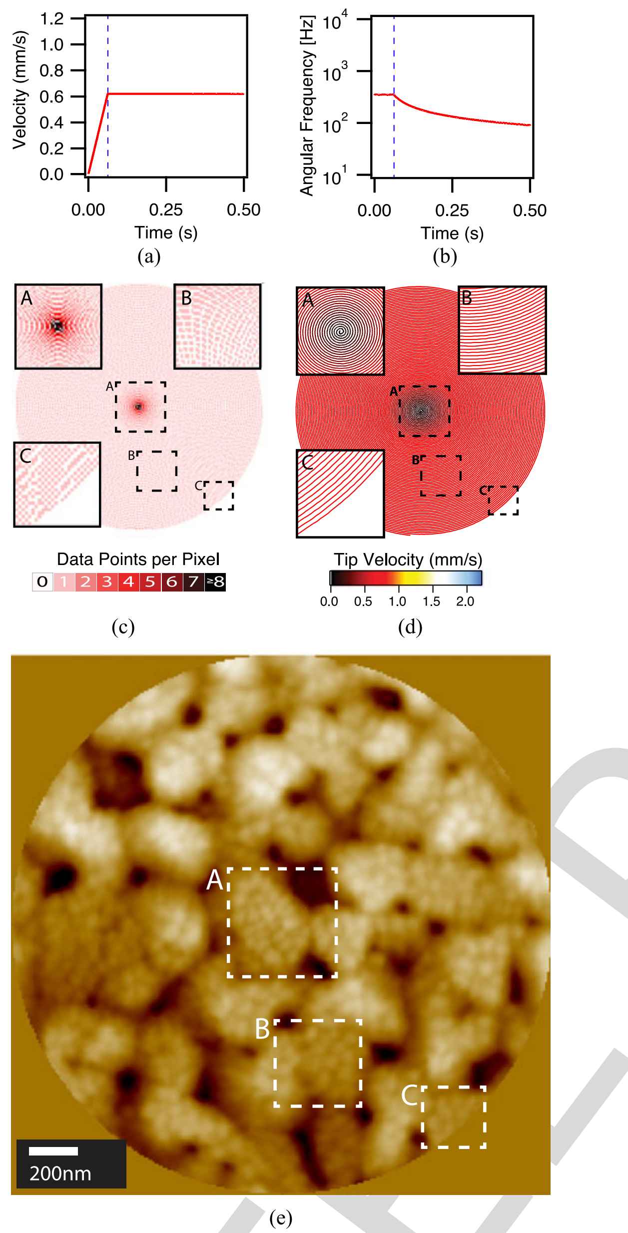

Fig. 4. Optimal Archimedean spiral (OPT). (a) Velocity as a function of scan time increases linearly and transitions to a constant value for the majority of the scan. (b) Angular frequency is held below the scanner distortion threshold before decreasing at large radius. (c) Theoretical data density is higher in the center due to the partial CAV scan but is mostly homogeneous. (d) Combining the best of both CLV and CAV spirals, the measured scan path and velocity match the theoretical values well. (e) A OPT image of copper evaporated onto annealed gold renders the sample well both in the center and at the periphery. The features in the boxes are compared with other scan waveforms in Fig. 5.

errors by exciting the scanner resonance. Also, the scan velocity should be slow enough that the Z-feedback loop accurately tracks all features. Other important criteria include that the data distribution should be generally homogeneous and if there are regions of higher density they should prioritize features of interest which are typically at the center of the image. Finally, adjacent segments of the scan should be scanned in the same direction. Otherwise delays in the positioning and the feedback loop cause the data to be inconsistent, causing irregularities in the image [37]. For example, this results in only trace or retrace data being used to create an image in raster scans and half the precious scan data are discarded. Spiral scans meet this last criterion quite well. This section contains an in-depth discussion of our results with the different Archimedean spirals followed by a comparison of their performance with more common waveforms (see Table I).

B. Constant Linear Velocity (CLV)

The CLV spiral meets all criteria satisfactorily except the first criterion for an ideal scan waveform. For the data density, Fig. 2(c), within the scan area, CLV spirals offer the lowest velocity possible, which is ideal for stable topography feedback. However, with high angular frequency in the center the excitation of the scanner resonance in the center is a significant failure. In Fig. 2(d), the error caused by the mechanical gain of the scanner is evident. The resonance is at 1600 Hz and has a Q of 5. Sweeping through the resonance with frequencies greater than 8 kHz causes the radius to became erroneously large in the center. As a result, there is no data in the center of the image. Our image inpainting algorithms aim to restore missing data. However, the scanner was whipped around violently enough during the chirp that the sensors became inaccurate and the intersecting loops have conflicting topography values for the same location. This resulted in the star-like artifacts that are very evident in the upper left of Fig. 5. It is possible to redeem the CLV spiral by making a donut-shaped scan [39] that removes the high-frequency portion, but then data are missing from the center of the scan where the features of interest likely are. We found CLV spiral to only be useful for the slowest of scans though we note that CLV may be crucial for some investigations, such as monitoring ferroelectric domain switching under a biased tip where the scan speed influences the switching probability and dynamics [40].

C. Constant Angular Velocity (CAV)

The CAV spiral better meets the criteria for an ideal scan waveform than the CLV spiral at these imaging speeds. This is mainly due to the fact that the highest frequency component of the waveform is 168 Hz, well below the scanner's resonance. For comparison, a raster scan of comparable data density would be 150 lines and a fast scan rate of 300 lines/s. Since at least three frequency components are required to make a satisfactory triangular waveform the 5th harmonic would be required at 1500 Hz, nine times higher than the CAV spiral scan while having over twice the velocity. The CAV spiral also has higher density data in the middle of the scan assuring that the most important features are well sampled and rendered. The main disadvantage of the CAV spiral is that the velocity is higher at the periphery reaching two times the average of a CLV spiral and approximately the same velocity of a raster scan over the same area. For the scan shown in Fig. 3, the maximum velocity $v_{\max}$ reaches ≈1.6 mm/s exceeding the limit for accurate imaging and lowering the homogeneity of the data ($\eta = 0.5$). This is

TABLE I
COMPARISON OF SCAN PERFORMANCE FOR VARIOUS SCAN PATHS

	Raster	Spirograph	Lissajous	CLV	CAV	OPT
1.1) Relative maximum angular frequency	>9.0	3.14	1.97	>50	1.0	2.1
1.2) Normalized std. dev. of angular frequency	—	0	0	1.17	0	0.51
2) Relative maximum speed	2.25	3.14	4.93	1.00	2.00	≈ 1.1
3.1) Relative average sample density	0.44	1.0	1.0	0.95	0.95	0.95
3.2) Relative maximum sample density	1	22	49	1	39	19
3.3) Percent pixels near average density	100	70	49	100	61	96
3.4) Data distribution prioritizes center	—	—	✗	—	√	√
4) Adjacent scan lines have same direction	√	✗	✗	√	√	√

Image area, resolution, and frame rate are the same for all waveforms and the values are scaled relative to each other for easy comparison. The table cells are shaded with red, yellow, and green for poor, satisfactory, and good performance, respectively. Optimal Archimedean spiral clearly has the best performance.

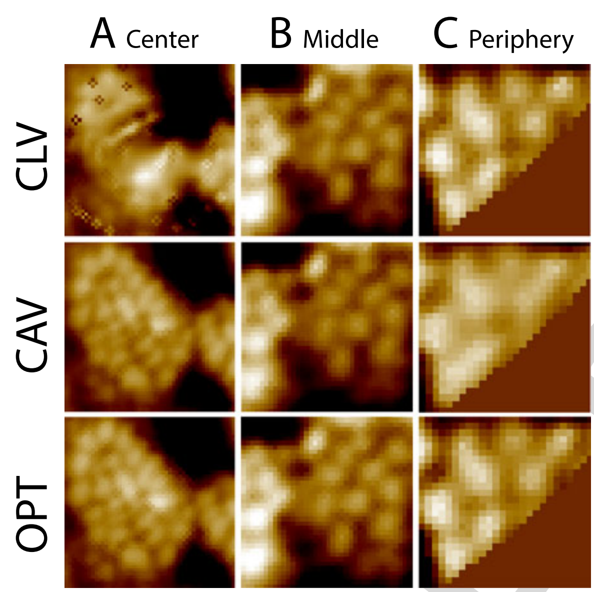

Fig. 5. Comparisons of CLV, CAV, and optimal Archimedean spiral scans showing the center, middle, and edge of the scans, respectively. The zoom-ins are specified by boxes A, B, and C in part (e) of Figs. 2, 3, and 4 and are 400, 300, and 200 nm, respectively. Color scales are enhanced compared with the original images. CLV fails in the center of the image and CAV blurs the periphery, while the OPT has the best performance throughout the scan.

evident in the center right of Fig. 5 where the height of the small copper grains is muted and some of the grains that are clearly resolved in the CLV spiral scan are joined together in the CAV scan. Resolving both the periphery and the center is preferable.

D. Optimal Archimedean Spiral (OPT)

The optimal Archimedean spiral starts with a CAV spiral in the center using a user specified maximum angular frequency, then transitions to a CLV spiral where the angular frequency decreases as the radius increases. The data shown here use an angular frequency limit of 350 Hz well below the resonance of the scanner leading to very even spacing between loops, as shown in Fig. 2(d). Like the CAV spiral, the OPT also has higher density data in the middle of the scan assuring that the most important features are well sampled and rendered. However, the transition to CLV spiral keeps the maximum velocity low and often very close to the speed represented by the CLV spiral. One may initially intuit that a high maximum angular frequency is good for the OPT so that the transition to CLV scan happens early in the scan and the maximum velocity is very close to the minimum velocity achieved by a CLV spiral. However, the maximum velocity increases moderately slowly initially as time to transition increases. For example, when transitioning at 40% of the scan time the maximum tip velocity is only 25% higher than a CLV spiral and the angular frequency starts only 24% higher than when using a CAV spiral.

The changing angular frequency that happens after the transition to CLV could cause distortions, such as dilation and twisting due to phase lag and changes in mechanical gain. Depending on imaging speed, sweeping through anomalies in the transfer function may be hard to avoid and artifacts may result. Fortunately, sensor inpainting mitigates such issues because the data are rendered from the measured position by the sensors. If the sensors are accurate then there should be no difference between images. On the instrument used for these experiments, we observed a 2% increase in the amplitude of the frequency response of the scanner near 400 Hz. This is enough for a few loops of data to be sparse then bunched as the frequency sweeps through the small peak and led us to choose a 350 Hz maximum for the angular frequency. In the frequency range of 150–350 Hz our frequency response was quite flat giving excellent results. Comparing the CAV and optimal Archimedean spiral images, Figs. 3 and 4, we find that there are positioning errors of 5 nm or about 0.2% of the scan size that are due to errors in accuracy of the sensors at the different frequencies used to scan the surface. These errors are negligible compared with what is frequently tolerated in AFM.

E. Comparison With Nonspiral Waveforms

Our optimal Archimedean spiral is significantly better suited for fast scanning than any other nonspiral waveform. We compare the performance of the different scan waveforms in Table I while holding image area, resolution, and frame rate constant. The specific values for the OPT scan in Table I depend on the value of t_{*L}. Here, we derive these values for $t_{*L} \approx 0.2$ as is used to gather the data, as shown in Fig. 4.

The maximum angular frequency measures how much the waveform stresses the *X*,*Y* scanner and the Lissajous, CAV, and OPT perform very well for this constraint. The standard deviation of the frequency is a proxy for the positioning errors due to a nonuniform scanner transfer function and inaccuracies of the sensor. The single frequency scans perform best here but the OPT scan is satisfactory especially if the time to transition is large.

The maximum speed measures how the waveform stresses the topography feedback loop. Using the equations found in Bazaei *et al.* [24] the maximum scan speed is a factor $\frac{\pi^2 a^2}{4t_{*L}}$ higher for a Lissajous scan than our OPT scan. For most imaging frame rates and maximum scan frequencies this is a substantial difference of over a factor of four! The CLV and OPT have the lowest velocity.

The average sample density shows how much data is discarded. Raster scans typically overshoot the displayed scan area and only use trace or retrace data for display. When developing spiral scans we initially used a waveform with the same number of loops to spiral back to the center. However, slight differences in amplitude or phase between spiraling in versus spiraling out can cause dilation of the images relative to each other such that there was a jitter when viewed sequentially. A satisfactory solution uses a few loops to spiral back to the center and discard these data (see Fig. 1 and Acknowledgment). For all the data presented here with $N = 85$ loops, less than 5% of the total scan time T is used for going back to the center leading to the 0.95 value compared with the Lissajous and Spirograph. Lissajous and Spirograph scans have coinciding start and endpoint of the scan waves which enables use of 100% of the data but both techniques require significantly higher maximum tip velocities than spiral scans. The maximum sample density reveals whether the scan moves slowly in places or crosses the same point multiple times. Percent pixels near average density measures if regions are homogeneously sampled. We score raster scan well even though it moves slowly during turn around because those data are excluded and already accounted for in the average sample density. Regarding sample density, CLV performs best if accurately executed with spirograph and OPT also rating well.

Having adjacent scan lines in the same direction is important so that signal delays are consistent across the image and do not cause artifacts or require discarding of data. When using contact mode, this requirement is more stringent. Friction forces cause twisting and bending of the cantilever. In this situation, artifacts may arise and the uniformly parallel scan lines during rastering can be advantageous but for ac modes the spirals are best. Here, we treat *X* and *Y* bandwidth as nearly equal which is not the case for all scanners. In tuning fork scanners, one axis is significantly faster and in this situation rastering would be favored [41] but for most scanners spirals will be best.

The optimal Archimedean spiral is able to cover the scan area in the shortest amount of time with the best balance of low angular frequency and low speed while having adjacent scan lines in the same direction and excellent data density in the middle. On the whole, the OPT fulfills all the criteria for an outstanding scan waveform. With a large scanner, we were able to image the sample with outstanding resolution at two frames per second. Reducing the scan area to 1.0 μm and maintaining the same spatial resolution and scanner frequency limits, the sample could have been imaged at nine frames per second. Implementing OPT on the smaller and lighter scanners that have been developed for high-speed AFM will lead to even faster scanning possibly an order of magnitude faster than raster scan. Optimal Archimedean spiral has near best performance for all important scan path criteria making it an ideal waveform.

VII. Conclusion

While many fields such as medical imaging [42] and astrophysics [43] utilize advanced image processing techniques to extend their capabilities, scanning probe techniques have been mired in the raster scan paradigm. Unlike raster scanning, where fast and slow scan axes exist, spiral scans evenly distribute the velocities to both *X* and *Y* axis. But in CLV spirals the highest angular frequencies can easily exceed the bandwidth of the *X*, *Y* positions sensors and thus result in a distorted image. Oppositely, very high tip velocities are required at the periphery of the scan area when maintaining constant angular frequency (CAV). When exceeding the bandwidth of the topographic feedback the high tip velocities can result in a blurred image and erroneous topographic data. The optimal Archimedean spiral is an ideal scan waveform for scanned probe microscopy respecting the instrument's limits for angular frequency and linear velocity it maintains an excellent data distribution and efficiently utilizes the scan time. This enables artifact free, high-resolution and high-quality imaging with few micron scan sizes and multiple frames per second on large heavy scanners.

Appendix

A. OPT Optimality

The scanning path is determined in polar coordinates by the angle $\theta(t) = 2\pi N g(t)$ and the radius $r(t) = Rg(t)$. The optimal parameterization of the spiral is a function g, which completes the scan in the least time subject to the physical constraints of the device. The constraints are given by

$$|\dot{g}| \leq \frac{\omega_L}{2\pi N} \equiv c_1 \tag{33}$$

and

$$|\dot{g}| \leq \frac{v_L}{R\sqrt{1 + (2\pi N g)^2}} \equiv c_2(g) \tag{34}$$

corresponding, respectively, to a frequency limitation of ω_L and a tip velocity limitation v_L. Define $l(g) \equiv \min(c_1, c_2(g))$, so that both constraints are conveniently stated by the condition $|\dot{g}| \leq l(g)$. Then, the optimal g minimize the scan time. The scan is finished when $g = 1$ when scanning counterclockwise or $g = -1$ when scanning clockwise. Taking the counterclockwise scenario, define the scan completion time by

$$T[g] = \min_{t \geq 0,\, g(t)=1} t.$$

The problem is to find a function g which, subject to the constraints, minimizes this quantity

$$g = \arg\min_{\hat{g} \in F} T[\hat{g}]$$

where F is the set of all continuously differentiable functions satisfying the constraint l

$$F = \left\{ h \in C^1([0, \infty]) : h(0) = 0, \dot{h} \leq l(h) \right\}.$$

Next we construct the optimal solution, then demonstrate optimality. Define g to be the solution to the differential equation $\dot{g} = l(g)$ with initial condition $g(0) = 0$. Because l is autonomous, uniformly Lipschitz, and bounded, the solution exists, is unique, and resides in F.

The parameterization given by g is fastest in the sense of $T[g]$. To see this, suppose $h \in F$ is another solution. Let $I = (a, b]$ be an interval such that $h(a) = g(a)$ and $h > g$ on I. If such an a and b do not exist it must be that $h \leq g$ for all time, so $T[h] \geq T[g]$ and h is not faster. Assume therefore a and b can be chosen. Within I there must be a point s at which $\dot{h}(s) > \dot{g}(s) \Rightarrow l(g(s)) < l(h(s))$, but this is impossible since $h(s) > g(s)$ and l decreases monotonically. No such interval I can exist, and therefore $T[h] \geq T[g]$. Because h was arbitrary there exists no strictly faster parameterization than g.

The analytic form of g is given by simple linear growth until $c_1 = c_2(g)$. Because of monotonic growth as well there is a single point t_L at which $c_1 = c_2(g(t_L))$, from which point onward the solution satisfies $\dot{g} = c_2(g)$, which is a member of the class of functions implicitly solving

$$\nu + \frac{v_L t}{R} = \frac{g(t)}{2}\sqrt{1 + (2\pi N g(t))^2} + \frac{\sinh^{-1}(2\pi N g(t))}{4\pi N}$$

for ν some constant depending on the value of $g(t_L)$. Provided that the approximations

$$N \gg 1$$

and

$$N g(t_L) \gg 1$$

hold, the 1 in the square root and the hyperbolic sine terms can be ignored thereby producing an approximate class of solutions of the form

$$g(t) = \frac{1}{\pi N}\sqrt{\nu + \frac{v_L t}{R}}.$$

The dimensionless parameterization f can now be defined as the scaled version of this optimal g using the total scan time $T = T[g]$.

ACKNOWLEDGMENT

The authors would like to thank the anonymous reviewers for their extremely careful reading of the manuscript and excellent suggestions as well as C. Callahan from Asylum Research an Oxford Instruments company for the suggestion to use a short spiral in.

REFERENCES

[1] G. Binnig, C. F. Quate, and C. Gerber, "Atomic force microscope," *Phys. Rev. Lett.*, vol. 56, pp. 930–933, Mar. 1986.
[2] L. Gross, F. Mohn, N. Moll, P. Liljeroth, and G. Meyer, "The chemical structure of a molecule resolved by atomic force microscopy," *Science*, vol. 325, no. 5944, pp. 1110–1114, 2009. [Online]. Available: http://www.sciencemag.org/content/325/5944/1110.abstract
[3] A. Noy, D. V. Vezenov, and C. M. Lieber, "Chemical force microscopy," *Annu. Rev. Mater. Sci.*, vol. 27, no. 1, pp. 381–421, 1997. [Online]. Available: http://dx.doi.org/10.1146/annurev.matsci.27.1.381
[4] P. D. Ashby and C. M. Lieber, "Ultra-sensitive imaging and interfacial analysis of patterned hydrophilic sam surfaces using energy dissipation chemical force microscopy," *J. Amer. Chem. Soc.*, vol. 127, no. 18, pp. 6814–6818, 2005. [Online]. Available: http://dx.doi.org/10.1021/ja0453127
[5] M. Nonnenmacher, M. P. O'Boyle, and H. K. Wickramasinghe, "Kelvin probe force microscopy," *Appl. Phys. Lett.*, vol. 58, no. 25, pp. 2921–2923, 1991. [Online]. Available: http://scitation.aip.org/content/aip/journal/apl/58/25/10.1063/1.105227
[6] D. Ziegler and A. Stemmer, "Force gradient sensitive detection in lift-mode kelvin probe force microscopy," *Nanotechnology*, vol. 22, no. 7, 2011, Art. no. 075501. [Online]. Available: http://stacks.iop.org/0957-4484/22/i=7/a=075501
[7] Y. Martin and H. Wickramasinghe, "Magnetic imaging by force microscopy with 1000 å resolution," *Appl. Phys. Lett.*, vol. 50, no. 20, pp. 1–3, 1987. [Online]. Available: http://scitation.aip.org/content/aip/journal/apl/50/20/10.1063/1.97800
[8] D. Carlton *et al.*, "Investigation of defects and errors in nanomagnetic logic circuits," *IEEE Trans. Nanotechnol.*, vol. 11, no. 4, pp. 760–762, Jul. 2012.
[9] P. K. Hansma, G. Schitter, G. E. Fantner, and C. Prater, "High-speed atomic force microscopy," *Science*, vol. 314, no. 5799, pp. 601–602, Oct. 2006. [Online]. Available: http://www.sciencemag.org/content/314/5799/601.short
[10] P. Kohli *et al.*, "High-speed atmospheric imaging of semiconductor wafers using rapid probe microscopy," *Proc. SPIE*, vol. 7971, pp. 797 119-1–797 119-9, 2011. [Online]. Available: http://dx.doi.org/10.1117/12.879456
[11] N. Kodera, D. Yamamoto, R. Ishikawa, and T. Ando, "Video imaging of walking myosin v by high-speed atomic force microscopy," *Nature*, vol. 468, no. 7320, pp. 72–76, Apr. 2010.
[12] T. Ando, N. Kodera, E. Takai, D. Maruyama, K. Saito, and A. Toda, "A high-speed atomic force microscope for studying biological macromolecules," *Proc. Nat. Acad. Sci.*, vol. 98, no. 22, pp. 12 468–12 472, 2001. [Online]. Available: http://www.pnas.org/content/98/22/12468.abstract
[13] T. Ando, T. Uchihashi, and T. Fukuma, "High-speed atomic force microscopy for nano-visualization of dynamic biomolecular processes," *Progr. Surf. Sci.*, vol. 83, no. 79, pp. 337–437, 2008.
[14] G. E. Fantner *et al.*, "Components for high speed atomic force microscopy," *Ultramicroscopy*, vol. 106, nos. 8/9, pp. 881–887, 2006.
[15] G. Schitter, P. Menold, H. F. Knapp, F. Allgower, and A. Stemmer, "High performance feedback for fast scanning atomic force microscopes," *Rev. Sci. Instrum.*, vol. 72, no. 8, pp. 3320–3327, 2001. [Online]. Available: http://scitation.aip.org/content/aip/journal/rsi/72/8/10.1063/1.1387253
[16] C. Braunsmann and T. E. Schaffer, "High-speed atomic force microscopy for large scan sizes using small cantilevers," *Nanotechnology*, vol. 21, no. 22, 2010, Art. no. 225705. [Online]. Available: http://stacks.iop.org/0957-4484/21/i=22/a=225705
[17] J. H. Kindt, G. E. Fantner, J. A. Cutroni, and P. K. Hansma, "Rigid design of fast scanning probe microscopes using finite element analysis," *Ultramicroscopy*, vol. 100, no. 34, pp. 259–265, 2004. [Online]. Available: http://www.sciencedirect.com/science/article/pii/S0304399104000385
[18] G. Schitter, P. J. Thurner, and P. K. Hansma, "Design and input-shaping control of a novel scanner for high-speed atomic force microscopy," *Mechatronics*, vol. 18, nos. 5/6, pp. 282–288, 2008. [Online]. Available: http://www.sciencedirect.com/science/article/pii/S0957415808000202
[19] A. D. L. Humphris, M. J. Miles, and J. K. Hobbs, "A mechanical microscope: High-speed atomic force microscopy," *Appl. Phys. Lett.*, vol. 86, no. 3, 2005, Art. no. 034106. [Online]. Available: http://scitation.aip.org/content/aip/journal/apl/86/3/10.1063/1.1855407
[20] L. M. Picco *et al.*, "Breaking the speed limit with atomic force microscopy," *Nanotechnology*, vol. 18, no. 4, 2007, Art. no. 044030. [Online]. Available: http://stacks.iop.org/0957-4484/18/i=4/a=044030

[21] T. Tuma, W. Haeberle, H. Rothuizen, J. Lygeros, A. Pantazi, and A. Sebastian, “A dual-stage nanopositioning approach to high-speed scanning probe microscopy,” in *Proc. 2012 IEEE 51st Annu. Conf. Decision Control*, Dec. 2012, pp. 5079–5084.

[22] Y. Zhou, G. Shang, W. Cai, and J.-e. Yao, “Cantilevered bimorph-based scanner for high speed atomic force microscopy with large scanning range,” *Rev. Sci. Instrum.*, vol. 81, no. 5, 2010, Art. no. 053708. [Online]. Available: http://scitation.aip.org/content/aip/journal/rsi/81/5/10.1063/1.3428731

[23] T. Tuma, J. Lygeros, V. Kartik, A. Sebastian, and A. Pantazi, “High-speed multiresolution scanning probe microscopy based on lissajous scan trajectories,” *Nanotechnology*, vol. 23, no. 18, 2012, Art. no. 185501. [Online]. Available: http://stacks.iop.org/0957-4484/23/i=18/a=185501

[24] A. Bazaei, Y. K. Yong, and S. O. R. Moheimani, “High-speed lissajous-scan atomic force microscopy: Scan pattern planning and control design issues,” *Rev. Sci. Instrum.*, vol. 83, no. 6, 2012, Art. no. 063701. [Online]. Available: http://scitation.aip.org/content/aip/journal/rsi/83/6/10.1063/1.4725525

[25] Y. K. Yong, S. O. R. Moheimani, and I. R. Petersen, “High-speed cycloid-scan atomic force microscopy,” *Nanotechnology*, vol. 21, no. 36, 2010, Art. no. 365503. [Online]. Available: http://stacks.iop.org/0957-4484/21/i=36/a=365503

[26] T. R. Meyer *et al.*, “Height drift correction in non-raster atomic force microscopy,” *Ultramicroscopy*, vol. 137, pp. 48–54, 2014. [Online]. Available: http://www.sciencedirect.com/science/article/pii/S0304399113002891

[27] M. Wieczorowski, “Spiral sampling as a fast way of data acquisition in surface topography,” *Int. J. Mach. Tools Manuf.*, vol. 41, no. 1314, pp. 2017–2022, 2001. [Online]. Available: http://www.sciencedirect.com/science/article/pii/S0890695501000669

[28] I. A. Mahmood and S. O. R. Moheimani, “Fast spiral-scan atomic force microscopy,” *Nanotechnology*, vol. 20, no. 36, 2009, Art. 365503. [Online]. Available: http://stacks.iop.org/0957-4484/20/i=36/a=365503

[29] S.-K. Hung, “Spiral scanning method for atomic force microscopy,” *J. Nanosci. Nanotechnol.*, vol. 10, no. 7, pp. 4511–4516, Jul. 2010. [Online]. Available: http://dx.doi.org/10.1166/jnn.2010.2353

[30] M. Rana, H. Pota, and I. Petersen, “Spiral scanning with improved control for faster imaging of AFM,” *IEEE Trans. Nanotechnol.*, vol. 13, no. 3, pp. 541–550, May 2014.

[31] I. Mahmood and S. Moheimani, “Spiral-scan atomic force microscopy: A constant linear velocity approach,” in *Proc. 10th IEEE Conf. Nanotechnol.*, Aug. 2010, pp. 115–120.

[32] X. Sang *et al.*, “Dynamic scan control in stem: spiral scans,” *Adv. Struct. Chem. Imag.*, vol. 2, no. 1, pp. 1–8, 2016. [Online]. Available: http://dx.doi.org/10.1186/s40679-016-0020-3

[33] M. Bertalmio, L. Vese, G. Sapiro, and S. Osher, “Simultaneous structure and texture image inpainting,” in *Proc. IEEE Comput. Soc. Conf. Comput. Vis. Pattern Recognit.*, Jun. 2003, vol. 2, pp. 707–712.

[34] T. Goldstein and S. Osher, “The split Bregman method for L1-regularized problems,” *SIAM J. Imag. Sci.*, vol. 2, no. 2, pp. 323–343, 2009.

[35] M. Bertalmio, G. Sapiro, V. Caselles, and C. Ballester, “Image inpainting,” in *Proc. 27th Annual Conf. Computer Graphics and Interactive Techniques* (Series SIGGRAPH ’00). New York, NY, USA: ACM Press, 2000, pp. 417–424.

[36] V. Caselles, J. Morel, and C. Sbert, “An axiomatic approach to image interpolation,” *IEEE Trans. Image Process.*, vol. 7, no. 3, pp. 376–386, Mar. 1998.

[37] D. Ziegler, T. R. Meyer, R. Farnham, C. Brune, A. L. Bertozzi, and P. D. Ashby, “Improved accuracy and speed in scanning probe microscopy by image reconstruction from non-gridded position sensor data,” *Nanotechnology*, vol. 24, no. 33, 2013, Art. no. 335703. [Online]. Available: http://stacks.iop.org/0957-4484/24/i=33/a=335703

[38] T. Tuma, J. Lygeros, A. Sebastian, and A. Pantazi, “Optimal scan trajectories for high-speed scanning probe microscopy,” in *Proc. 2012 Amer. Control Conf.*, Jun. 2012, pp. 3791–3796.

[39] D. Momotenko, J. C. Byers, K. McKelvey, M. Kang, and P. R. Unwin, “High-speed electrochemical imaging,” *ACS Nano*, vol. 9, no. 9, pp. 8942–8952, 2015. [Online]. Available: http://dx.doi.org/10.1021/acsnano.5b02792

[40] B. D. Huey, R. Nath Premnath, S. Lee, and N. A. Polomoff, “High speed SPM applied for direct nanoscale mapping of the influence of defects on ferroelectric switching dynamics,” *J. Amer. Ceramic Soc.*, vol. 95, no. 4, pp. 1147–1162, 2012. [Online]. Available: http://dx.doi.org/10.1111/j.1551-2916.2012.05099.x

[41] A. D. L. Humphris, J. K. Hobbs, and M. J. Miles, “Ultrahigh-speed scanning near-field optical microscopy capable of over 100 frames per second,” *Appl. Phys. Lett.*, vol. 83, no. 1, pp. 6–8, 2003. [Online]. Available: http://scitation.aip.org/content/aip/journal/apl/83/1/10.1063/1.1590737

[42] J. H. Lee, B. A. Hargreaves, B. S. Hu, and D. G. Nishimura, “Fast 3D imaging using variable-density spiral trajectories with applications to limb perfusion,” *Magn. Resonance Med.*, vol. 50, no. 6, pp. 1276–1285, 2003. [Online]. Available: http://dx.doi.org/10.1002/mrm.10644

[43] J.-L. Starck, “Sparse astronomical data analysis,” in *Statistical Challenges in Modern Astronomy V* (Series Lecture Notes in Statistics), vol. 902, E. D. Feigelson and G. J. Babu, Eds. New York, NY, USA: Springer-Verlag, 2012, pp. 239–253. [Online]. Available: http://dx.doi.org/10.1007/978-1-4614-3520-4_23

Dominik Ziegler was born in Switzerland, in 1977. He studied at the University of Neuchtel, Neuchtel, Switzerland, and received the M.S. degree in microengineering from École Polytechnique Fdrale de Lausanne, Lausanne, Switzerland, in 2003. After visiting the Biohybrid Systems Laboratory, University of Tokyo, Japan, he received the Ph.D. degree in the Nanotechnology Group, ETH Zurich, Zurich, Switzerland, in 2009.

His research interests include advanced research in micro- and nano-fabrication, bio-MEMS, lab-on-a-chip, and general low-noise scientific instrumentation. His work on scanning probe microscopes focuses on Kelvin probe force microscopy and high-speed applications. As a Postdoctoral Researcher in the Lawrence Berkeley National Laboratory, Berkeley, CA, USA, he developed high-speed techniques using spiral scanning and developed encased cantilevers for more sensitive measurements in liquids. Co-founding Scuba Probe Technologies LLC his work currently focuses on the commercialization of encased cantilevers. Since 2016, he also directs research activities at the Politehnica University of Bucharest, Romania.

Travis R. Meyer received the B.Sc. degree in physics and the B.A. degree in applied mathematics from the University of California, Los Angeles (UCLA), CA, USA, in 2011. He is currently a graduate student working toward the Ph.D. degree in applied mathematics at UCLA.

His interests include variational models for machine learning and data processing, specifically in the domains of signal and text analysis. In addition to his research, he has worked in collaboration with specialists in a variety of domains as well as helped in developing and instructing a machine learning course for the UCLA Mathematics Department.

Andreas Amrein was born in Aarau, Switzerland, in 1989. He received the B.Sc. degree in mechanical engineering and the M.Sc. degree in robotics, systems, and control from the Swiss Federal Institute of Technology, Zurich, Switzerland, in 2013 and 2016, respectively.

From 2014 to 2015, he was with the Lawrence Berkeley National Laboratory. He recently joined Eulitha AG, where he works on photolithographic systems as a Product Development Engineer.

Andrea L. Bertozzi received the B.A., M.A., and Ph.D. degrees in mathematics all from Princeton University, Princeton, NJ, USA, in 1987, 1988, and 1991, respectively.

She was with the faculty of the University of Chicago, Chicago, IL, USA, from 1991 to 1995 and of the Duke University, Durham, NC, USA, from 1995 to 2004. From 1995 to 1996, she was the Maria Goeppert-Mayer Distinguished Scholar at Argonne National Laboratory. Since 2003, she has been with the University of California, Los Angeles, as a Professor of mathematics, and currently serves as the Director of applied mathematics. In 2012, she was appointed the Betsy Wood Knapp Chair for Innovation and Creativity. Her research interests include machine learning, image processing, cooperative control of robotic vehicles, swarming, fluid interfaces, and crime modeling.

Dr. Bertozzi is a Fellow of both the Society for Industrial and Applied Mathematics and the American Mathematical Society; she is a Member of the American Physical Society. She has served as a Plenary/Distinguished Lecturer for both SIAM and AMS and is an Associate Editor for the SIAM journals: *Multiscale Modelling and Simulation*, *Imaging Sciences*, and *Mathematical Analysis*. She also serves on the editorial board of *Interfaces and Free Boundaries*, *Nonlinearity*, *Applied Mathematics Letters*, *Journal of the American Mathematical Society*, *Journal of Nonlinear Science*, *Journal of Statistical Physics*, and *Communications in Mathematical Sciences*. She received the Sloan Foundation Research Fellowship, the Presidential Career Award for Scientists and Engineers, and the SIAM Kovalevsky Prize in 2009.

Paul D. Ashby received the B.Sc. degree in chemistry from Westmont College, Santa Barbara, CA, USA, in 1996 and the Ph.D. degree in physical chemistry from Harvard University, Cambridge, MA, USA, in 2003.

Subsequently, he was part of the founding of the Molecular Foundry, Lawrence Berkeley National Laboratory, Berkeley, CA, USA, as a jump-start Postdoc and transitioned into a Staff Scientist position, in 2007. His research aims to understand the *in situ* properties of soft dynamic materials, such as polymers, biomaterials, and living systems and frequently utilizes scanned probe methods. Recent endeavors include the development of encased cantilevers for gentle imaging in fluid and high-speed AFM scanning. He is a Cofounder of Scuba Probe Technologies LLC.

Queries

Q1. Author: Please check first footnote as set for correctness.

Ideal Scan Path for High-Speed Atomic Force Microscopy

Dominik Ziegler, Travis R. Meyer, Andreas Amrein, Andrea L. Bertozzi, and Paul D. Ashby

***Abstract*—We propose a new scan waveform ideally suited for high-speed atomic force microscopy. It is an optimization of the Archimedean spiral scan path with respect to the *X,Y* scanner bandwidth and scan speed. The resulting waveform uses a constant angular velocity spiral in the center and transitions to constant linear velocity toward the periphery of the scan. We compare it with other scan paths and demonstrate that our novel spiral best satisfies the requirements of high-speed atomic force microscopy by utilizing the scan time most efficiently with excellent data density and data distribution. For accurate *X,Y*, and *Z* positioning our proposed scan pattern has low angular frequency and low linear velocities that respect the instruments mechanical limits. Using sensor inpainting we show artifact-free high-resolution images taken at two frames per second with a 2.2 μm scan size on a moderately large scanner capable of 40 μm scans.**

***Index Terms*—Actuators, atomic force microscopy (AFM), motion control.**

I. Introduction

ATOMIC force microscopy (AFM) techniques acquire high-resolution images by scanning a sharp tip over a sample while measuring the interaction between the tip and sample [1]. AFM has the ability to image material surfaces with exquisite resolution [2]. Furthermore, careful probe design facilitates nanoscale measurement of specific physical or chemical properties, such as surface energy [3], [4] or electrostatic [5], [6] and magnetic [7], [8] forces. Therefore, AFM has become one of the most frequently used characterization tools in nanoscience. However, the sequential nature of scanning limits the speed of data acquisition and most instruments take several minutes to obtain a high-quality image. The productivity and use of AFM would increase dramatically if the speed could match the imaging speeds of other scanning microscopes, such as confocal and scanning electron microscopes [9]. The semiconductor industry, which requires detection of nanoscopic defects over large areas, is an important driver for higher scan speeds [10]. More importantly, higher temporal resolution enables the exploration of dynamic chemical and biomolecular processes [11]. This is especially important for dynamic nanoscale phenomena of materials that are sensitive to the radiation associated with light and electron microscopy making AFM the best characterization tool.

Significant engineering effort over the last decade has pushed the speed limits of AFM to a few frames per second [12]–[15]. Most researchers operate within the raster scan paradigm, where the tip is moved in a zig-zag pattern over the sample at a constant speed in the image area. The rationale for the raster pattern is that with regular sampling and constant scanner velocity image rendering is simple because the data points align with the pixels of the image spatially. However, achieving accurate images is challenging because piezoelectric nanopositioners have notoriously nonlinear displacement response and the mechanical resonances of the high-inertia scanner amplify the harmonics of the waveform that are required to create the turnaround region of the raster scan. Working within the raster scan paradigm, most methods to speed up the AFM have focused on the mechanical design. The most common means to build fast scanners is to reduce the size of the scanner and increase stiffness [16]–[22] so that the scanner actuates effectively at higher frequencies but this places strict limitations on the mass of the sample.

Using nonraster scan waveforms with low-frequency components provides an opportunity to increase imaging speed. Lissajous scans have been shown to be advantageous for high-speed scanning because they can cover the entire scan area using a sinusoidal scan pattern of constant amplitude and frequency [23], [24]. Similarly, cycloid [25] and spirograph [26] scans use a single frequency circular scan with a constant offset between adjacent loops.

In this paper, we analyze the suitability of spiral scan paths for high-speed scanning. Having constant distance between loops makes Archimedean spirals especially useful. They can be performed either using constant angular velocity (CAV) [27]–[30] or constant linear velocity (CLV) [31], [32]. At least a twofold increase in temporal or spatial resolution is achieved over raster scanning because, when generating an image, almost 100% of the data is used instead of throwing away trace or retrace data. Furthermore, spiral scan patterns require less bandwidth and

Manuscript received March 3, 2016; revised July 2, 2016; accepted August 21, 2016. Recommended by Technical Editor G. Cherubini. This work was supported in part by the National Science Foundation under Grant DMS-1118971, in part by the Office of Naval Research under Grant N000141210838, in part by the Small Business Innovation Research Phase I and II Grants under Award DE-SC 0013212, and in part by the National Science Foundation under Award 1556128. The work at Molecular Foundry was supported by the Office of Science, Office of Basic Energy Sciences, U.S. Department of Energy under Contract DE-AC02-05CH11231.

D. Ziegler is with the Molecular Foundry, Lawrence Berkeley National Laboratory, Berkeley, CA 94720 USA, and also with the Scuba Probe Technologies LLC, Alameda, CA 94501 USA (e-mail: dziegler@lbl.gov).

A. Amrein and P. D. Ashby are with the Molecular Foundry, Lawrence Berkeley National Laboratory, Berkeley, CA 94720 USA (e-mail: andi.amrein@gmail.com; pdashby@lbl.gov).

T. R. Meyer and A. L. Bertozzi are with the Department of Mathematics, University of California Los Angeles, Los Angeles, CA 90095 USA (e-mail: euphopiab@gmail.com; bertozzi@math.ucla.edu).

Color versions of one or more of the figures in this paper are available online at http://ieeexplore.ieee.org.

Digital Object Identifier 10.1109/TMECH.2016.2615327

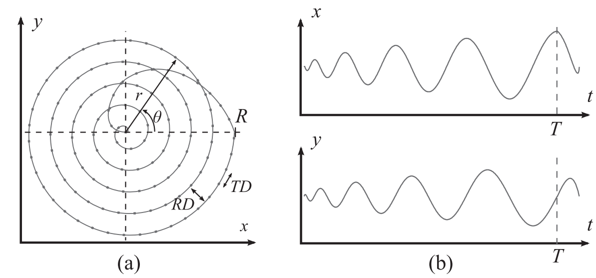

Fig. 1. (a) Illustration of an Archimedean spiral showing outward and truncated inward scan paths to quickly return to the starting point at the origin. For clarity only a small number of loops of $N = 5$ is used in the outward spiral. The radial and tangential sampling distances are specified by RD and TD, respectively. (b) Transforming r and θ into Cartesian coordinates gives the *X* and *Y* motion of the piezo. The vertical dotted line at time T marks the transition from outward scan to the truncated inward scan.

are better suited to drive high-inertia nanopositioners for fast scanning. However, most of today's nonraster scan attempts use sensors to steer the probe over the sample using a closed-loop configuration. This slows down the achievable frame rates. We have shown that ultimate control over the position is not required for accurate imaging. When sensors detect the position, an accurate image can be reconstructed using inpainting algorithms [33]–[36] from data recorded along any arbitrary open-loop path. The technique, which we call sensor inpainting [37], frees AFM from the paradigm of raster scanning and the need for slower closed-loop control of scanner position. We have used sensor inpainting to render images from Archimedean spiral and spirograph scan patterns [26], [37].

In this paper, we analyze Archimedean spiral scan patterns for their suitability for fast scanning. We propose a new Archimedean spiral, which we call the optimal spiral, that combines the benefits of CAV and CLV scans. The proposed spiral scan follows an Archimedean scan path but respects the mechanical limits of the instrument by balancing velocity and angular frequency to obtain the optimum data distribution for accurate high-speed scanning when scan velocity needs to be minimized.

II. Description of Scan Path

A. Tip Velocity and Angular Velocity

Fig. 1(a) shows an example of Archimedean spiral with five loops for the outward path and a fast inward path to return to the starting point at the origin. We describe the outward scan pattern using polar coordinates $r(t)$ and $\theta(t)$ as functions of the scan time. The time required to complete the outward scan is T and t_* is the dimensionless quantity $t_* = t/T$

$$r = Rf(t_*) \tag{1}$$

$$\theta = 2\pi N f(t_*) \tag{2}$$

where N is the number of loops and R is the desired radius. To fully scan the circular area, it is required that $f(0) = 0$ and $f(1) = 1$, but in principle $f(t_*)$ can be of any arbitrary shape. When eliminating the temporal function one obtains the polar expression of an Archimedean spiral in the form of

$$r(\theta) = \frac{R\theta}{2\pi N}. \tag{3}$$

In an Archimedean spiral, the scan radius r increases by a constant pitch R/N for each full revolution, and the maximal scan radius R is reached exactly after N full loops. Experimentally, the scan pattern applied to the piezo is achieved by transforming r and θ into Cartesian coordinates [see Fig. 1(b)].

The tip velocity v_s and angular velocity $\dot{\theta}$ are given by

$$v_s(r,\theta) = \sqrt{(r\dot{\theta})^2 + \dot{r}^2} \tag{4}$$

$$v_s(t_*) = \frac{Rf'(t_*)}{T}\sqrt{(2\pi N f(t_*))^2 + 1} \tag{5}$$

$$\dot{\theta}(t_*) = \frac{2\pi N}{T} f'(t_*). \tag{6}$$

We denote the derivative with respect to time t with a dot and the derivative with respect to t_* with a prime.

B. Data Density and Data Distribution

The Archimedean spirals analyzed here have different functions for $f(t_*)$ such that they follow the same scan path, but with different tip velocities. As a consequence, different data point distributions result when using a constant sampling frequency F_s. Fig. 1(a) shows the sampling along the spiral path and the radial distance (RD) and tangential distance (TD) between data points. The general expressions for radial distance (RD) and tangential distance (TD) are given by

$$\mathrm{RD}(r,\theta) = \frac{2\pi\dot{r}}{\dot{\theta}},\ \mathrm{TD}(r,\theta) = \frac{r\dot{\theta}}{F_s}. \tag{7}$$

The local data density δ is expressed by the inverse of the product of TD and RD and represents the samples per unit area as

$$\delta(r) = \frac{1}{\mathrm{TD}\cdot\mathrm{RD}} = \frac{F_s}{2\pi r\dot{r}} \tag{8}$$

$$\delta(t_*) = \frac{n}{2\pi R^2 f(t_*) f'(t_*)} \tag{9}$$

where n is the number of samples, $n = F_s T$. Having uniform density throughout the image is ideal for maximizing the information being measured from the sample. Furthermore, it is important to have good homogeneity η of the sample density, i.e., an even distribution of the data points in all directions. The ratio of RD to TD describes such homogeneity by comparing the spacing between data points

$$\eta(r,\theta) = \frac{\mathrm{RD}}{\mathrm{TD}} = \frac{2\pi F_s \dot{r}}{(\dot{\theta})^2 r} \tag{10}$$

$$\eta(t_*) = \frac{n}{2\pi N^2 f(t_*) f'(t_*)}. \tag{11}$$

As discussed in earlier work [37] when using isotropic inpainting algorithms such as heat equation, $\eta = 1$ results in the best rendering with least artifacts.

By definition Archimedean spirals have constant RD, and the density δ and homogeneity η simplify to

$$\delta(r,\theta) = \frac{NF_s}{Rr\dot{\theta}}, \quad \eta(r,\theta) = \frac{F_s R}{Nr\dot{\theta}}. \tag{12}$$

III. CLV Spiral

An Archimedean spiral with essentially constant velocity along the scan path is the result of $f(t_*)=\sqrt{t_*}$ [see Fig. 2(a)]. For this case, the tip velocity is given by

$$v_{s_{\mathrm{CLV}}}(t_*) = \frac{R\sqrt{(2\pi N)^2 t_* + 1}}{2T\sqrt{t_*}} \approx \frac{\pi N R}{T}. \tag{13}$$

Toward the very center of the image $v_{s_{\mathrm{CLV}}}$ theoretically approaches infinity. In discrete implementations, however, the velocity decreases [see Fig. 2(a)] because the high frequencies for small r in the position signal are lost due to the spacing of samples. When $t_* \gg 1/(2\pi N)^2$ the velocity rapidly approaches a constant. Similarly, toward the very center of the image, the angular frequency function goes to infinity

$$\dot{\theta}(t_*)_{\mathrm{CLV}} = \frac{\pi N}{T\sqrt{t_*}} \tag{14}$$

except for the discrete implementation. To maintain CLV angular frequency more than two orders of magnitudes higher in the center than on the periphery of the image is required [see Fig. 2(b)]. Note that the area under the velocity curve [see Fig. 2(a)] represents the total arc length ($\approx$0.3 mm), while the area under the angular frequency curve [see Fig. 2(b)] corresponds to the number of loops $N = 85$. These values remain constant for all spiral scans described here.

The expressions for density δ_{CLV} and η_{CLV} are independent of time t_* and radius r and simplify to

$$\delta_{\mathrm{CLV}} \approx \frac{n}{\pi R^2} \tag{15}$$

$$\eta_{\mathrm{CLV}} \approx \frac{n}{\pi N^2}. \tag{16}$$

We imaged a sample of copper evaporated onto annealed gold because the contrast in size between the copper and gold grains creates high information content. This makes this sample an ideal image to test the accuracy of the data collection and rendering when scanning quickly. The sample has complex features of different sizes and the smallest feature resolvable by the tip is $\approx$25 nm. We used a Cypher ES by Oxford Instruments equipped with a piezoelectric scanner having 40 μm range in *X* and *Y*, 4 μm range in *Z*, and low-noise position sensors. While using a contact mode in constant height mode we used a sampling frequency F_s of 50 kHz to impose limited bandwidth on the data collection as if we were operating with force feedback and were limited by the *z*-feedback loop and tip–sample interaction. This makes the data and analysis most relevant to the majority of AFM performed in constant force mode. The scan is 2.2 μm in size with $N = 85$ loops and collected in 0.5 s producing a scan velocity of 600 mm/s. Using the Nyquist criterion for information content, the $\approx$25 nm feature size, and 50 kHz sampling frequency, we calculate that $v_s \approx$625 mm/s should be the scan speed limit for accurate imaging. Constant δ and η,

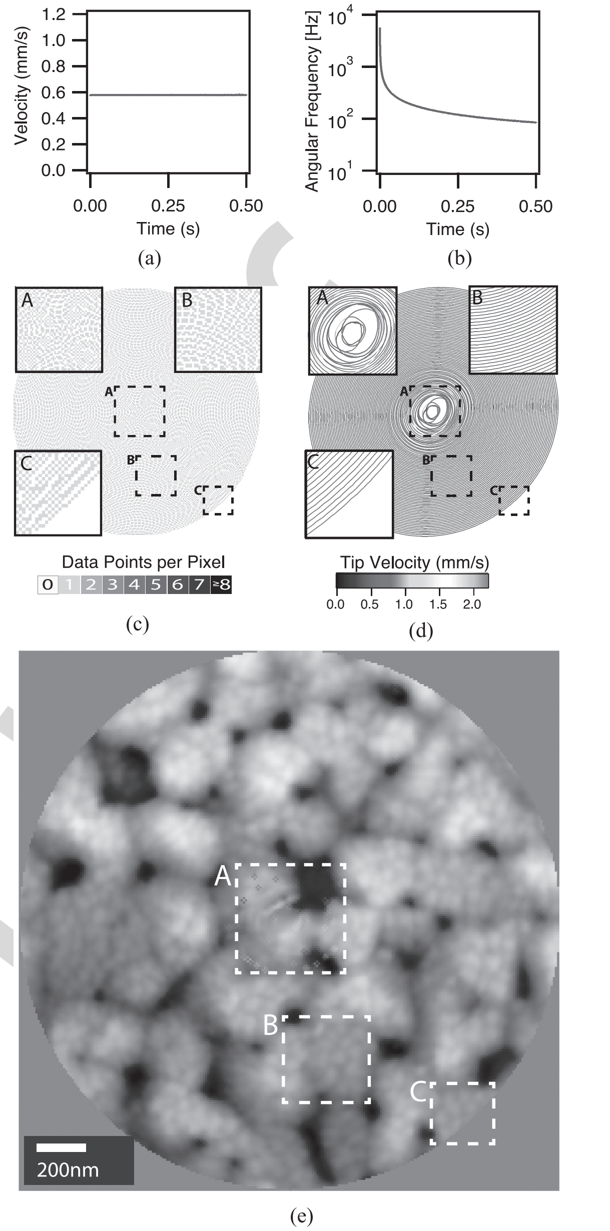

Fig. 2. CLV spiral. (a) Velocity as a function of scan time is constant. (b) To maintain constant speed at small radii the angular frequency “blows up” to values exceeding the resonance frequency of the scanner. (c) Theoretical spatial data density distribution showing number of samples per pixel in the rendered image. (d) Scan path, as measured with the sensors, during the CLV spiral scan. Color scale represents velocity of the scanner. (e) A CLV image of copper evaporated onto annealed gold. The relatively slow scan speed and excellent sample density at the outer edge of the image lead to good fidelity of the features. The features in the boxes (A, B, C) are compared with other scan waveforms in Fig. 5.

resulting from theoretical constant velocity v_s and sampling F_s produces an ideal dataset with $n = 25$ k data points. In the density map, Fig. 2(c), the color represents the number of recorded data points that fall within each pixel. All collected deflection data points are inpainted within a circular image with a diameter of 256 pixels containing about 50k pixels. The insets are magnifications of the center (A), middle (B), and periphery (C) of the scan showing that the data density is the same throughout the scan. At most each pixel contains one data point. The insets show the great homogeneity of the data distribution resulting for CLV scans.

The scan path measured by the sensors on the scanner is shown in Fig. 2(d) and it is slightly oblong from lower left to upper right. The high angular frequencies used in the center of the scan exceed 8 kHz and excite the resonance of the scanner. This increases the radius causing poor sampling in the center of the scan and erratic motion as evidenced by the very fast motion of greater than 2 mm/s [see Fig. 2(d) inset A]. The CLV spiral scan of the copper/gold sample is shown in Fig. 2(e). We used sensor inpainting [37] to create a 2.0 μm round image, 256 pixels wide, which trimmed the data and used ≈20 kS such that there are ≈ 0.25 data points per pixel. The CLV scan captures the features of the sample very well except in the center where there is obvious distortion and artifacts from driving at very high angular frequency. Therefore, in order to prevent distortions in the image, the angular velocity is required to match the bandwidth of the scanner.

IV. CAV Spiral

CAV scans drive the piezos at a single frequency. This helps to prevent the above-mentioned distortions due to the resonances of the scanner. CAV scans use the simplest linear function

$$f(t_*) = t_* \tag{17}$$

where the resulting angular velocity, Fig. 3(b), is simply given by the number of revolutions in the total time

$$\dot{\theta}(t_*)_{\mathrm{CAV}} = \frac{2\pi N}{T}. \tag{18}$$

The velocity $v_{s_{\mathrm{CAV}}}$ increases nearly linearly with time for CAV spirals as the radius increases. The function for scan velocity

$$v_{s_{\mathrm{CAV}}}(t_*) = \frac{R}{T}\sqrt{4(\pi N t_*)^2 + 1} \approx \frac{2\pi N R}{T} t_* \tag{19}$$

simplifies to a linear function of t_*, for almost all of the scan, as shown in Fig. 3(a).

Using (1), (8), (10), and (17) the expressions for data density δ and homogeneity η simplify to the following radial dependencies:

$$\delta(r)_{\mathrm{CAV}} \approx \frac{n}{2\pi R r} \tag{20}$$

$$\eta(r)_{\mathrm{CAV}} \approx \frac{nR}{2\pi N^2 r}. \tag{21}$$

Data density for a CAV spiral scan with similar scan parameters as those used for Fig. 2 is shown in Fig. 3(c). Because the scan velocity is near zero at the center of the image the data density is extremely high reaching 74 samples in the center pixels. Conversely the data density δ becomes sparse toward the periphery. Since the scan time T and number of loops N are the same as the CLV scan [see Fig. 2(c)], the average value of η is also one but the value drops to 0.5 at the periphery where features start to be undersampled. We imaged the copper/gold sample in the same location as Fig. 2(e) using a CAV spiral. The measured scan path, Fig. 3(d), has very even spacing radially because the scanner responds with constant mechanical gain and phase lag when driven at constant angular frequency. The measured velocity matches the theoretical values well. The inpainted image is shown in Fig. 3(e). The features in the center of the image are reproduced well due to the slow angular frequency, high sampling, and η but the periphery is under sampled and the features become blurred.

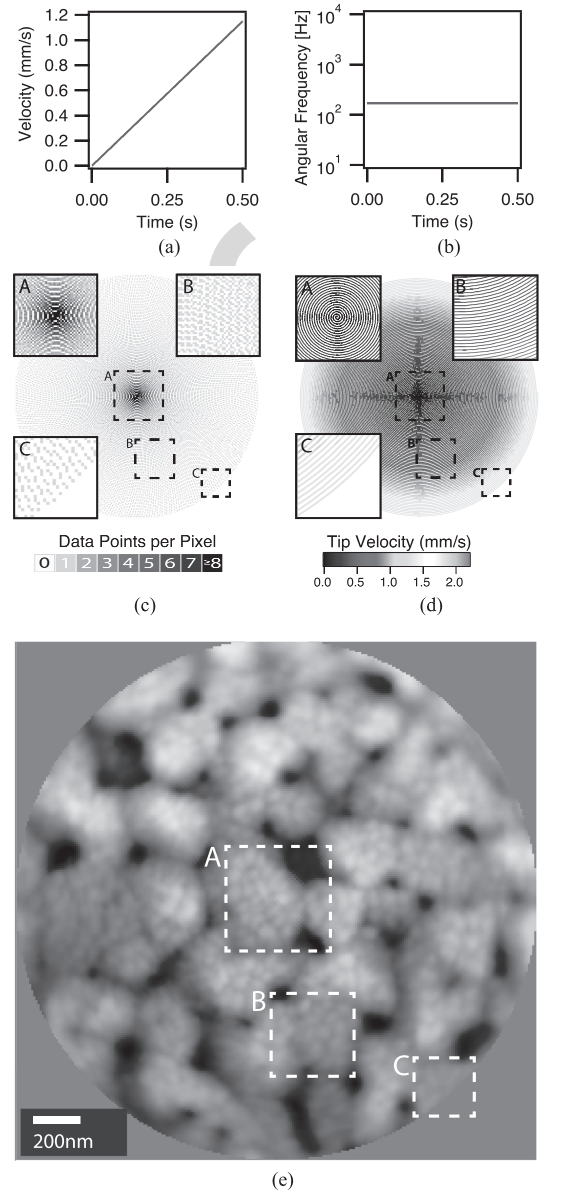

Fig. 3. CAV spiral. (a) Velocity as a function of scan time increases linearly and (b) angular frequency is constant. (c) Theoretical data density is very high in the center and getting sparse toward the periphery. (d) The velocity is low in the middle and high on the periphery. (e) CAV image of copper evaporated onto annealed gold at same location as Fig. 2. The CAV eliminates errors in the center of the image but the high linear velocity and sparse data at the edges smears out features. The features in the boxes are compared with other scan waveforms in Fig. 5.

The need to capture the information at the periphery of the image determines the sampling rate and velocity for CAV spirals. Therefore, for most of the scan, near the center, the instrument is going too slow and wasting precious time. Neither CLV nor CAV spirals are ideal for imaging the sample quickly but each has properties that are advantageous. The optimal Archimedean spiral combines the advantages of both.

V. Optimal Archimedean Spiral (OPT)

The ideal Archimedean spiral would have the shortest scan times while respecting the instrument's mechanical limits. The time function $f(t_*)$ of the Archimedean spiral can be any arbitrary shape leading to various scan speeds and frequencies. As observed in Fig. 2, the mechanical gain of the resonance can lead to large excursions from the intended scan path and inaccuracies. It is best if the *X*,*Y* scan frequencies stay well below the resonance. Similarly, high tip speeds lead to sparse data, Fig. 3, or high tip–sample forces from poor *Z*-piezo feedback making tip speed an equally important optimization parameter.

We solved for the optimal time function $f(t_*)$ using maximum *X*,*Y* scan frequency ω_L and tip speed v_L as limiting criteria. The complete optimization is found in Appendix 1 and has similarities with the optimization method of Tuma *et al.* [38]. The resulting waveform follows ω_L in the center of the scan and then follows v_L at the periphery. Effectively, the waveform combines the benefits of CAV and CLV scans. We call the new scan waveform the optimal Archimedean spiral (OPT).

The optimal Archimedean spiral is the fastest Archimedean spiral that respects the limits of *X*,*Y* scanner bandwidth and scan speed. In our experience, the parameter of scan time and scan speed are equally valid independent variables for the parameterization of the OPT so we also present a parameterization that follows the optimal principle of performing CAV in the center and CLV at the periphery but uses scan time as an independent variable.

The CLV is produced when $f(t_*) = \sqrt{t_*}$ and the CAV is produced when $f(t_*) = t_*$ with t_* dimensionless time. Let the angular frequency limit of the AFM be given by $\frac{d\theta}{dt} \le \omega_L$. Define $a \equiv \frac{2\pi N}{T\omega_L}$. To push the angular frequency limit initially the composite spiral's f must be of the form $f(t_*) = \frac{t_*}{a}$ as this results in $\frac{d\theta}{dt} = \omega_L$. Using the CAV up to sometime t_{*L} then transitioning to a CLV spiral with parameters C_1 and C_2 means the optimum Archimedean spiral has a function f of the form

$$f(t_*) = \begin{cases} \frac{t_*}{a} & \text{if } t_* \le t_{*L} \\ \sqrt{C_1 t_* + C_2} & \text{if } t_* > t_{*L}. \end{cases} \tag{22}$$

To find the parameters, t_{*L}, C_1, and C_2, we enforce three properties of the final spiral. The scan should be finished at time $t_* = 1$ hence $f(1) = 1$ and f and f' should be continuous at t_{*L}.

The three conditions imply, in order, the equations

$$1 = \sqrt{C_1 + C_2} \tag{23}$$

$$\frac{t_{*L}}{a} = \sqrt{C_1 t_{*L} + C_2} \tag{24}$$

$$\frac{1}{a} = \frac{C_1}{2}(C_1 t_{*L} + C_2)^{-\frac{1}{2}}. \tag{25}$$

The first equation implies $C_2 = 1 - C_1$ and substituting (24) into (25) yields

$$\frac{1}{a} = \frac{C_1 a}{2t_{*L}}. \tag{26}$$

Therefore,

$$C_1 = \frac{2t_{*L}}{a^2} \tag{27}$$

$$C_2 = 1 - \frac{2t_{*L}}{a^2} \tag{28}$$

which after substituting into (24) produces a quadratic equation in t_{*L}:

$$0 = t_{*L}^2 - 2t_{*L} + a^2 \tag{29}$$

$$\Rightarrow t_{*L} = 1 \pm \sqrt{1 - a^2}. \tag{30}$$

The discriminant is positive provided $a < 1$, which is violated only when the scan cannot be completed in the given time subject to the given angular frequency limit. As the transition must take place in the scan time $t_{*L} \in [0, 1]$ the negative sign is the natural solution hence

$$t_{*L} = 1 - \sqrt{1 - a^2} \tag{31}$$

is the transition time t_{*L}.

According to (5), the speed of the tip for this f at time t_{*L} is

$$v(t_{*L}) = \frac{R}{aT}\sqrt{1 + \left(\frac{2\pi N}{a}\right)^2 t_{*L}^2} \approx \frac{\pi N R}{T}\frac{2t_{*L}}{a^2}. \tag{32}$$

The velocity curve for an optimal Archimedean spiral scan is shown in Fig. 4(a). The velocity increases linearly and quickly because the angular frequency is at the limit. When the normalized time t_* reaches t_{*L} the scan transitions to CLV with constant velocity and decreasing angular frequency, as shown in Fig. 4(b). The density image, shown in Fig. 4(c), is mostly homogeneous throughout. At the center, inset A, the data density is high because of the short section of CAV spiral but otherwise samples are evenly spread over the whole image, insets B and C, where η is very close to one. We again imaged the copper/gold sample in the same location as Fig. 2(e) but using an OPT spiral of the same time, number of loops, and sampling rate. Like the CAV spiral, the scan path is evenly spaced throughout the image but the velocity is always low, as shown in Fig. 4(d). The features throughout the image are reproduced well showing the superior performance of the OPT, as shown in Fig. 4(e).

VI. Discussion

A. Further Criteria for Comparing Waveforms

Increasing the frame rate of scanning probe techniques is essential for capturing dynamic processes at the nanoscale. Here we introduce design criteria that allow further comparison of various scan waveforms to determine the best scan wave for fast scanning. As we already mentioned in the optimization to create the OPT waveform, the scan must respect the mechanical bandwidth of the *X*,*Y* scanner, i.e., the scan waveform needs to have sufficiently low angular frequency to avoid positioning

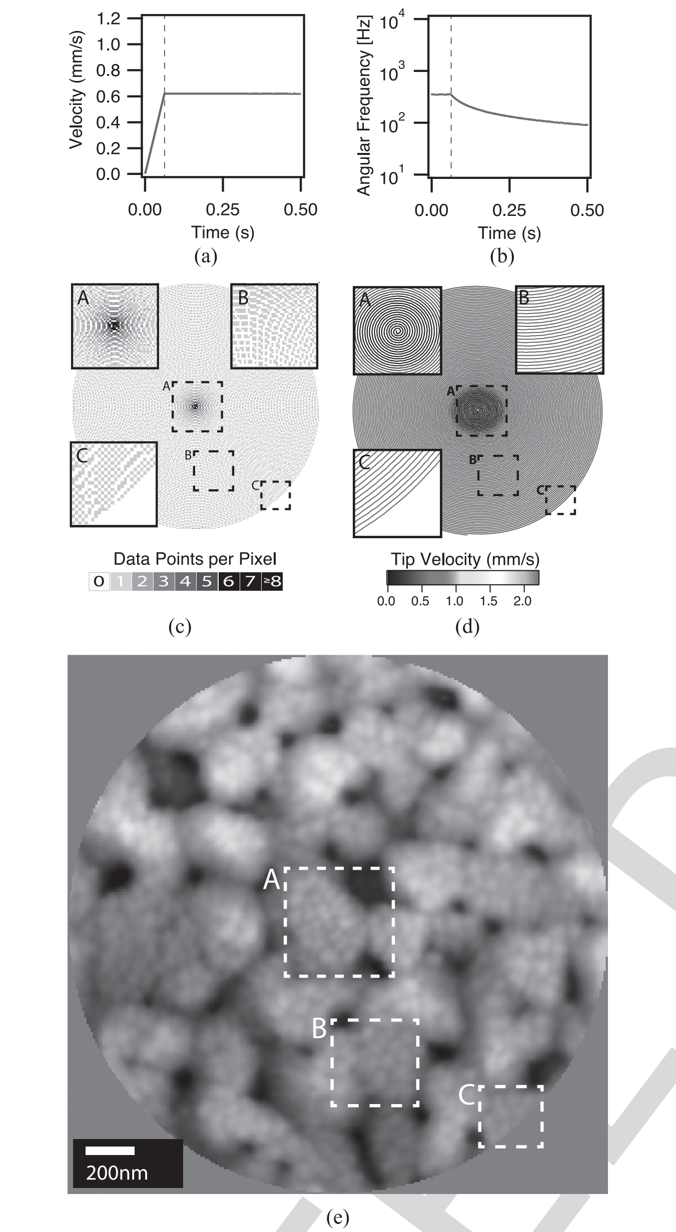

Fig. 4. Optimal Archimedean spiral (OPT). (a) Velocity as a function of scan time increases linearly and transitions to a constant value for the majority of the scan. (b) Angular frequency is held below the scanner distortion threshold before decreasing at large radius. (c) Theoretical data density is higher in the center due to the partial CAV scan but is mostly homogeneous. (d) Combining the best of both CLV and CAV spirals, the measured scan path and velocity match the theoretical values well. (e) A OPT image of copper evaporated onto annealed gold renders the sample well both in the center and at the periphery. The features in the boxes are compared with other scan waveforms in Fig. 5.

errors by exciting the scanner resonance. Also, the scan velocity should be slow enough that the Z-feedback loop accurately tracks all features. Other important criteria include that the data distribution should be generally homogeneous and if there are regions of higher density they should prioritize features of interest which are typically at the center of the image. Finally, adjacent segments of the scan should be scanned in the same direction. Otherwise delays in the positioning and the feedback loop cause the data to be inconsistent, causing irregularities in the image [37]. For example, this results in only trace or retrace data being used to create an image in raster scans and half the precious scan data are discarded. Spiral scans meet this last criterion quite well. This section contains an in-depth discussion of our results with the different Archimedean spirals followed by a comparison of their performance with more common waveforms (see Table I).

B. Constant Linear Velocity (CLV)

The CLV spiral meets all criteria satisfactorily except the first criterion for an ideal scan waveform. For the data density, Fig. 2(c), within the scan area, CLV spirals offer the lowest velocity possible, which is ideal for stable topography feedback. However, with high angular frequency in the center the excitation of the scanner resonance in the center is a significant failure. In Fig. 2(d), the error caused by the mechanical gain of the scanner is evident. The resonance is at 1600 Hz and has a Q of 5. Sweeping through the resonance with frequencies greater than 8 kHz causes the radius to became erroneously large in the center. As a result, there is no data in the center of the image. Our image inpainting algorithms aim to restore missing data. However, the scanner was whipped around violently enough during the chirp that the sensors became inaccurate and the intersecting loops have conflicting topography values for the same location. This resulted in the star-like artifacts that are very evident in the upper left of Fig. 5. It is possible to redeem the CLV spiral by making a donut-shaped scan [39] that removes the high-frequency portion, but then data are missing from the center of the scan where the features of interest likely are. We found CLV spiral to only be useful for the slowest of scans though we note that CLV may be crucial for some investigations, such as monitoring ferroelectric domain switching under a biased tip where the scan speed influences the switching probability and dynamics [40].

C. Constant Angular Velocity (CAV)

The CAV spiral better meets the criteria for an ideal scan waveform than the CLV spiral at these imaging speeds. This is mainly due to the fact that the highest frequency component of the waveform is 168 Hz, well below the scanner's resonance. For comparison, a raster scan of comparable data density would be 150 lines and a fast scan rate of 300 lines/s. Since at least three frequency components are required to make a satisfactory triangular waveform the 5th harmonic would be required at 1500 Hz, nine times higher than the CAV spiral scan while having over twice the velocity. The CAV spiral also has higher density data in the middle of the scan assuring that the most important features are well sampled and rendered. The main disadvantage of the CAV spiral is that the velocity is higher at the periphery reaching two times the average of a CLV spiral and approximately the same velocity of a raster scan over the same area. For the scan shown in Fig. 3, the maximum velocity $v_{\max}$ reaches $\approx$1.6 mm/s exceeding the limit for accurate imaging and lowering the homogeneity of the data ($\eta = 0.5$). This is

TABLE I
COMPARISON OF SCAN PERFORMANCE FOR VARIOUS SCAN PATHS

	Raster	Spirograph	Lissajous	CLV	CAV	OPT
1.1) Relative maximum angular frequency	>9.0	3.14	1.97	>50	1.0	2.1
1.2) Normalized std. dev. of angular frequency	—	0	0	1.17	0	0.51
2) Relative maximum speed	2.25	3.14	4.93	1.00	2.00	≈ 1.1
3.1) Relative average sample density	0.44	1.0	1.0	0.95	0.95	0.95
3.2) Relative maximum sample density	1	22	49	1	39	19
3.3) Percent pixels near average density	100	70	49	100	61	96
3.4) Data distribution prioritizes center	—	—	✗	—	√	√
4) Adjacent scan lines have same direction	√	✗	✗	√	√	√

Image area, resolution, and frame rate are the same for all waveforms and the values are scaled relative to each other for easy comparison. The table cells are shaded with red, yellow, and green for poor, satisfactory, and good performance, respectively. Optimal Archimedean spiral clearly has the best performance.

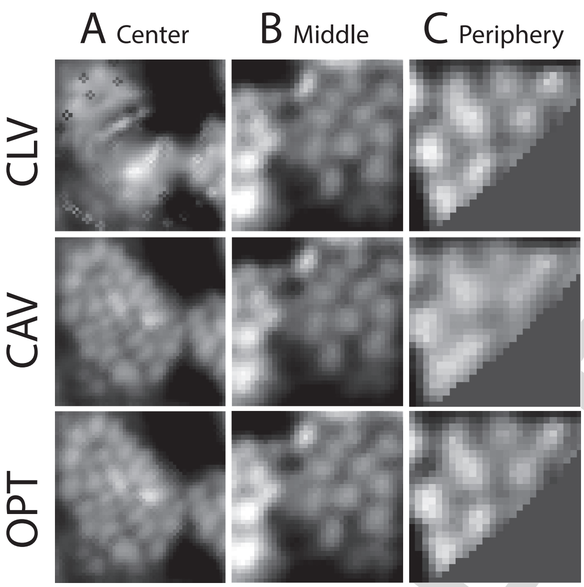

Fig. 5. Comparisons of CLV, CAV, and optimal Archimedean spiral scans showing the center, middle, and edge of the scans, respectively. The zoom-ins are specified by boxes A, B, and C in part (e) of Figs. 2, 3, and 4 and are 400, 300, and 200 nm, respectively. Color scales are enhanced compared with the original images. CLV fails in the center of the image and CAV blurs the periphery, while the OPT has the best performance throughout the scan.

evident in the center right of Fig. 5 where the height of the small copper grains is muted and some of the grains that are clearly resolved in the CLV spiral scan are joined together in the CAV scan. Resolving both the periphery and the center is preferable.

D. Optimal Archimedean Spiral (OPT)

The optimal Archimedean spiral starts with a CAV spiral in the center using a user specified maximum angular frequency, then transitions to a CLV spiral where the angular frequency decreases as the radius increases. The data shown here use an angular frequency limit of 350 Hz well below the resonance of the scanner leading to very even spacing between loops, as shown in Fig. 2(d). Like the CAV spiral, the OPT also has higher density data in the middle of the scan assuring that the most important features are well sampled and rendered. However, the transition to CLV spiral keeps the maximum velocity low and often very close to the speed represented by the CLV spiral. One may initially intuit that a high maximum angular frequency is good for the OPT so that the transition to CLV scan happens early in the scan and the maximum velocity is very close to the minimum velocity achieved by a CLV spiral. However, the maximum velocity increases moderately slowly initially as time to transition increases. For example, when transitioning at 40% of the scan time the maximum tip velocity is only 25% higher than a CLV spiral and the angular frequency starts only 24% higher than when using a CAV spiral.

The changing angular frequency that happens after the transition to CLV could cause distortions, such as dilation and twisting due to phase lag and changes in mechanical gain. Depending on imaging speed, sweeping through anomalies in the transfer function may be hard to avoid and artifacts may result. Fortunately, sensor inpainting mitigates such issues because the data are rendered from the measured position by the sensors. If the sensors are accurate then there should be no difference between images. On the instrument used for these experiments, we observed a 2% increase in the amplitude of the frequency response of the scanner near 400 Hz. This is enough for a few loops of data to be sparse then bunched as the frequency sweeps through the small peak and led us to choose a 350 Hz maximum for the angular frequency. In the frequency range of 150–350 Hz our frequency response was quite flat giving excellent results. Comparing the CAV and optimal Archimedean spiral images, Figs. 3 and 4, we find that there are positioning errors of 5 nm or about 0.2% of the scan size that are due to errors in accuracy of the sensors at the different frequencies used to scan the surface. These errors are negligible compared with what is frequently tolerated in AFM.

E. Comparison With Nonspiral Waveforms

Our optimal Archimedean spiral is significantly better suited for fast scanning than any other nonspiral waveform. We compare the performance of the different scan waveforms in Table I while holding image area, resolution, and frame rate constant. The specific values for the OPT scan in Table I depend on the value of t_{*L}. Here, we derive these values for $t_{*L} \approx 0.2$ as is used to gather the data, as shown in Fig. 4.

The maximum angular frequency measures how much the waveform stresses the *X*,*Y* scanner and the Lissajous, CAV, and OPT perform very well for this constraint. The standard deviation of the frequency is a proxy for the positioning errors due to a nonuniform scanner transfer function and inaccuracies of the sensor. The single frequency scans perform best here but the OPT scan is satisfactory especially if the time to transition is large.

The maximum speed measures how the waveform stresses the topography feedback loop. Using the equations found in Bazaei *et al.* [24] the maximum scan speed is a factor $\frac{\pi^2 a^2}{4t_{*L}}$ higher for a Lissajous scan than our OPT scan. For most imaging frame rates and maximum scan frequencies this is a substantial difference of over a factor of four! The CLV and OPT have the lowest velocity.

The average sample density shows how much data is discarded. Raster scans typically overshoot the displayed scan area and only use trace or retrace data for display. When developing spiral scans we initially used a waveform with the same number of loops to spiral back to the center. However, slight differences in amplitude or phase between spiraling in versus spiraling out can cause dilation of the images relative to each other such that there was a jitter when viewed sequentially. A satisfactory solution uses a few loops to spiral back to the center and discard these data (see Fig. 1 and Acknowledgment). For all the data presented here with $N = 85$ loops, less than 5% of the total scan time T is used for going back to the center leading to the 0.95 value compared with the Lissajous and Spirograph. Lissajous and Spirograph scans have coinciding start and endpoint of the scan waves which enables use of 100% of the data but both techniques require significantly higher maximum tip velocities than spiral scans. The maximum sample density reveals whether the scan moves slowly in places or crosses the same point multiple times. Percent pixels near average density measures if regions are homogeneously sampled. We score raster scan well even though it moves slowly during turn around because those data are excluded and already accounted for in the average sample density. Regarding sample density, CLV performs best if accurately executed with spirograph and OPT also rating well.

Having adjacent scan lines in the same direction is important so that signal delays are consistent across the image and do not cause artifacts or require discarding of data. When using contact mode, this requirement is more stringent. Friction forces cause twisting and bending of the cantilever. In this situation, artifacts may arise and the uniformly parallel scan lines during rastering can be advantageous but for ac modes the spirals are best. Here, we treat *X* and *Y* bandwidth as nearly equal which is not the case for all scanners. In tuning fork scanners, one axis is significantly faster and in this situation rastering would be favored [41] but for most scanners spirals will be best.

The optimal Archimedean spiral is able to cover the scan area in the shortest amount of time with the best balance of low angular frequency and low speed while having adjacent scan lines in the same direction and excellent data density in the middle. On the whole, the OPT fulfills all the criteria for an outstanding scan waveform. With a large scanner, we were able to image the sample with outstanding resolution at two frames per second. Reducing the scan area to 1.0 μm and maintaining the same spatial resolution and scanner frequency limits, the sample could have been imaged at nine frames per second. Implementing OPT on the smaller and lighter scanners that have been developed for high-speed AFM will lead to even faster scanning possibly an order of magnitude faster than raster scan. Optimal Archimedean spiral has near best performance for all important scan path criteria making it an ideal waveform.

VII. Conclusion

While many fields such as medical imaging [42] and astrophysics [43] utilize advanced image processing techniques to extend their capabilities, scanning probe techniques have been mired in the raster scan paradigm. Unlike raster scanning, where fast and slow scan axes exist, spiral scans evenly distribute the velocities to both *X* and *Y* axis. But in CLV spirals the highest angular frequencies can easily exceed the bandwidth of the *X*, *Y* positions sensors and thus result in a distorted image. Oppositely, very high tip velocities are required at the periphery of the scan area when maintaining constant angular frequency (CAV). When exceeding the bandwidth of the topographic feedback the high tip velocities can result in a blurred image and erroneous topographic data. The optimal Archimedean spiral is an ideal scan waveform for scanned probe microscopy respecting the instrument's limits for angular frequency and linear velocity it maintains an excellent data distribution and efficiently utilizes the scan time. This enables artifact free, high-resolution and high-quality imaging with few micron scan sizes and multiple frames per second on large heavy scanners.

Appendix

A. OPT Optimality

The scanning path is determined in polar coordinates by the angle $\theta(t) = 2\pi N g(t)$ and the radius $r(t) = Rg(t)$. The optimal parameterization of the spiral is a function g, which completes the scan in the least time subject to the physical constraints of the device. The constraints are given by

$$|\dot{g}| \leq \frac{\omega_L}{2\pi N} \equiv c_1 \tag{33}$$

and

$$|\dot{g}| \leq \frac{v_L}{R\sqrt{1 + (2\pi N g)^2}} \equiv c_2(g) \tag{34}$$

corresponding, respectively, to a frequency limitation of ω_L and a tip velocity limitation v_L. Define $l(g) \equiv \min(c_1, c_2(g))$, so that both constraints are conveniently stated by the condition $|\dot{g}| \leq l(g)$. Then, the optimal g minimize the scan time. The scan is finished when $g = 1$ when scanning counterclockwise or $g = -1$ when scanning clockwise. Taking the counterclockwise scenario, define the scan completion time by

$$T[g] = \min_{t \geq 0, g(t)=1} t.$$

The problem is to find a function g which, subject to the constraints, minimizes this quantity

$$g = \arg\min_{\hat{g} \in F} T[\hat{g}]$$

where F is the set of all continuously differentiable functions satisfying the constraint l

$$F = \left\{ h \in C^1([0, \infty]) : h(0) = 0, \dot{h} \le l(h) \right\}.$$

Next we construct the optimal solution, then demonstrate optimality. Define g to be the solution to the differential equation $\dot{g} = l(g)$ with initial condition $g(0) = 0$. Because l is autonomous, uniformly Lipschitz, and bounded, the solution exists, is unique, and resides in F.

The parameterization given by g is fastest in the sense of $T[g]$. To see this, suppose $h \in F$ is another solution. Let $I = (a, b]$ be an interval such that $h(a) = g(a)$ and $h > g$ on I. If such an a and b do not exist it must be that $h \le g$ for all time, so $T[h] \ge T[g]$ and h is not faster. Assume therefore a and b can be chosen. Within I there must be a point s at which $\dot{h}(s) > \dot{g}(s) \Rightarrow l(g(s)) < l(h(s))$, but this is impossible since $h(s) > g(s)$ and l decreases monotonically. No such interval I can exist, and therefore $T[h] \ge T[g]$. Because h was arbitrary there exists no strictly faster parameterization than g.

The analytic form of g is given by simple linear growth until $c_1 = c_2(g)$. Because of monotonic growth as well there is a single point t_L at which $c_1 = c_2(g(t_L))$, from which point onward the solution satisfies $\dot{g} = c_2(g)$, which is a member of the class of functions implicitly solving

$$\nu + \frac{v_L t}{R} = \frac{g(t)}{2}\sqrt{1 + (2\pi N g(t))^2} + \frac{\sinh^{-1}(2\pi N g(t))}{4\pi N}$$

for ν some constant depending on the value of $g(t_L)$. Provided that the approximations

$$N \gg 1$$

and

$$N g(t_L) \gg 1$$

hold, the 1 in the square root and the hyperbolic sine terms can be ignored thereby producing an approximate class of solutions of the form

$$g(t) = \frac{1}{\pi N}\sqrt{\nu + \frac{v_L t}{R}}.$$

The dimensionless parameterization f can now be defined as the scaled version of this optimal g using the total scan time $T = T[g]$.

Acknowledgment

The authors would like to thank the anonymous reviewers for their extremely careful reading of the manuscript and excellent suggestions as well as C. Callahan from Asylum Research an Oxford Instruments company for the suggestion to use a short spiral in.

References

[1] G. Binnig, C. F. Quate, and C. Gerber, "Atomic force microscope," *Phys. Rev. Lett.*, vol. 56, pp. 930–933, Mar. 1986.

[2] L. Gross, F. Mohn, N. Moll, P. Liljeroth, and G. Meyer, "The chemical structure of a molecule resolved by atomic force microscopy," *Science*, vol. 325, no. 5944, pp. 1110–1114, 2009. [Online]. Available: http://www.sciencemag.org/content/325/5944/1110.abstract

[3] A. Noy, D. V. Vezenov, and C. M. Lieber, "Chemical force microscopy," *Annu. Rev. Mater. Sci.*, vol. 27, no. 1, pp. 381–421, 1997. [Online]. Available: http://dx.doi.org/10.1146/annurev.matsci.27.1.381

[4] P. D. Ashby and C. M. Lieber, "Ultra-sensitive imaging and interfacial analysis of patterned hydrophilic sam surfaces using energy dissipation chemical force microscopy," *J. Amer. Chem. Soc.*, vol. 127, no. 18, pp. 6814–6818, 2005. [Online]. Available: http://dx.doi.org/10.1021/ja0453127

[5] M. Nonnenmacher, M. P. O'Boyle, and H. K. Wickramasinghe, "Kelvin probe force microscopy," *Appl. Phys. Lett.*, vol. 58, no. 25, pp. 2921–2923, 1991. [Online]. Available: http://scitation.aip.org/content/aip/journal/apl/58/25/10.1063/1.105227

[6] D. Ziegler and A. Stemmer, "Force gradient sensitive detection in lift-mode kelvin probe force microscopy," *Nanotechnology*, vol. 22, no. 7, 2011, Art. no. 075501. [Online]. Available: http://stacks.iop.org/0957-4484/22/i=7/a=075501

[7] Y. Martin and H. Wickramasinghe, "Magnetic imaging by force microscopy with 1000 å resolution," *Appl. Phys. Lett.*, vol. 50, no. 20, pp. 1–3, 1987. [Online]. Available: http://scitation.aip.org/content/aip/journal/apl/50/20/10.1063/1.97800

[8] D. Carlton *et al.*, "Investigation of defects and errors in nanomagnetic logic circuits," *IEEE Trans. Nanotechnol.*, vol. 11, no. 4, pp. 760–762, Jul. 2012.

[9] P. K. Hansma, G. Schitter, G. E. Fantner, and C. Prater, "High-speed atomic force microscopy," *Science*, vol. 314, no. 5799, pp. 601–602, Oct. 2006. [Online]. Available: http://www.sciencemag.org/content/314/5799/601.short

[10] P. Kohli *et al.*, "High-speed atmospheric imaging of semiconductor wafers using rapid probe microscopy," *Proc. SPIE*, vol. 7971, pp. 797 119-1–797 119-9, 2011. [Online]. Available: http://dx.doi.org/10.1117/12.879456

[11] N. Kodera, D. Yamamoto, R. Ishikawa, and T. Ando, "Video imaging of walking myosin v by high-speed atomic force microscopy," *Nature*, vol. 468, no. 7320, pp. 72–76, Apr. 2010.

[12] T. Ando, N. Kodera, E. Takai, D. Maruyama, K. Saito, and A. Toda, "A high-speed atomic force microscope for studying biological macromolecules," *Proc. Nat. Acad. Sci.*, vol. 98, no. 22, pp. 12 468–12 472, 2001. [Online]. Available: http://www.pnas.org/content/98/22/12468.abstract

[13] T. Ando, T. Uchihashi, and T. Fukuma, "High-speed atomic force microscopy for nano-visualization of dynamic biomolecular processes," *Progr. Surf. Sci.*, vol. 83, no. 79, pp. 337–437, 2008.

[14] G. E. Fantner *et al.*, "Components for high speed atomic force microscopy," *Ultramicroscopy*, vol. 106, nos. 8/9, pp. 881–887, 2006.

[15] G. Schitter, P. Menold, H. F. Knapp, F. Allgower, and A. Stemmer, "High performance feedback for fast scanning atomic force microscopes," *Rev. Sci. Instrum.*, vol. 72, no. 8, pp. 3320–3327, 2001. [Online]. Available: http://scitation.aip.org/content/aip/journal/rsi/72/8/10.1063/1.1387253

[16] C. Braunsmann and T. E. Schaffer, "High-speed atomic force microscopy for large scan sizes using small cantilevers," *Nanotechnology*, vol. 21, no. 22, 2010, Art. no. 225705. [Online]. Available: http://stacks.iop.org/0957-4484/21/i=22/a=225705

[17] J. H. Kindt, G. E. Fantner, J. A. Cutroni, and P. K. Hansma, "Rigid design of fast scanning probe microscopes using finite element analysis," *Ultramicroscopy*, vol. 100, no. 34, pp. 259–265, 2004. [Online]. Available: http://www.sciencedirect.com/science/article/pii/S0304399104000385

[18] G. Schitter, P. J. Thurner, and P. K. Hansma, "Design and input-shaping control of a novel scanner for high-speed atomic force microscopy," *Mechatronics*, vol. 18, nos. 5/6, pp. 282–288, 2008. [Online]. Available: http://www.sciencedirect.com/science/article/pii/S0957415808000202

[19] A. D. L. Humphris, M. J. Miles, and J. K. Hobbs, "A mechanical microscope: High-speed atomic force microscopy," *Appl. Phys. Lett.*, vol. 86, no. 3, 2005, Art. no. 034106. [Online]. Available: http://scitation.aip.org/content/aip/journal/apl/86/3/10.1063/1.1855407

[20] L. M. Picco *et al.*, "Breaking the speed limit with atomic force microscopy," *Nanotechnology*, vol. 18, no. 4, 2007, Art. no. 044030. [Online]. Available: http://stacks.iop.org/0957-4484/18/i=4/a=044030

[21] T. Tuma, W. Haeberle, H. Rothuizen, J. Lygeros, A. Pantazi, and A. Sebastian, "A dual-stage nanopositioning approach to high-speed scanning probe microscopy," in *Proc. 2012 IEEE 51st Annu. Conf. Decision Control*, Dec. 2012, pp. 5079–5084.

[22] Y. Zhou, G. Shang, W. Cai, and J.-e. Yao, "Cantilevered bimorph-based scanner for high speed atomic force microscopy with large scanning range," *Rev. Sci. Instrum.*, vol. 81, no. 5, 2010, Art. no. 053708. [Online]. Available: http://scitation.aip.org/content/aip/journal/rsi/81/5/10.1063/1.3428731

[23] T. Tuma, J. Lygeros, V. Kartik, A. Sebastian, and A. Pantazi, "High-speed multiresolution scanning probe microscopy based on lissajous scan trajectories," *Nanotechnology*, vol. 23, no. 18, 2012, Art. no. 185501. [Online]. Available: http://stacks.iop.org/0957-4484/23/i=18/a=185501

[24] A. Bazaei, Y. K. Yong, and S. O. R. Moheimani, "High-speed lissajous-scan atomic force microscopy: Scan pattern planning and control design issues," *Rev. Sci. Instrum.*, vol. 83, no. 6, 2012, Art. no. 063701. [Online]. Available: http://scitation.aip.org/content/aip/journal/rsi/83/6/10.1063/1.4725525

[25] Y. K. Yong, S. O. R. Moheimani, and I. R. Petersen, "High-speed cycloid-scan atomic force microscopy," *Nanotechnology*, vol. 21, no. 36, 2010, Art. no. 365503. [Online]. Available: http://stacks.iop.org/0957-4484/21/i=36/a=365503

[26] T. R. Meyer *et al.*, "Height drift correction in non-raster atomic force microscopy," *Ultramicroscopy*, vol. 137, pp. 48–54, 2014. [Online]. Available: http://www.sciencedirect.com/science/article/pii/S0304399113002891

[27] M. Wieczorowski, "Spiral sampling as a fast way of data acquisition in surface topography," *Int. J. Mach. Tools Manuf.*, vol. 41, no. 1314, pp. 2017–2022, 2001. [Online]. Available: http://www.sciencedirect.com/science/article/pii/S0890695501000669

[28] I. A. Mahmood and S. O. R. Moheimani, "Fast spiral-scan atomic force microscopy," *Nanotechnology*, vol. 20, no. 36, 2009, Art. 365503. [Online]. Available: http://stacks.iop.org/0957-4484/20/i=36/a=365503

[29] S.-K. Hung, "Spiral scanning method for atomic force microscopy," *J. Nanosci. Nanotechnol.*, vol. 10, no. 7, pp. 4511–4516, Jul. 2010. [Online]. Available: http://dx.doi.org/10.1166/jnn.2010.2353

[30] M. Rana, H. Pota, and I. Petersen, "Spiral scanning with improved control for faster imaging of AFM," *IEEE Trans. Nanotechnol.*, vol. 13, no. 3, pp. 541–550, May 2014.

[31] I. Mahmood and S. Moheimani, "Spiral-scan atomic force microscopy: A constant linear velocity approach," in *Proc. 10th IEEE Conf. Nanotechnol.*, Aug. 2010, pp. 115–120.

[32] X. Sang *et al.*, "Dynamic scan control in stem: spiral scans," *Adv. Struct. Chem. Imag.*, vol. 2, no. 1, pp. 1–8, 2016. [Online]. Available: http://dx.doi.org/10.1186/s40679-016-0020-3

[33] M. Bertalmio, L. Vese, G. Sapiro, and S. Osher, "Simultaneous structure and texture image inpainting," in *Proc. IEEE Comput. Soc. Conf. Comput. Vis. Pattern Recognit.*, Jun. 2003, vol. 2, pp. 707–712.

[34] T. Goldstein and S. Osher, "The split Bregman method for L1-regularized problems," *SIAM J. Imag. Sci.*, vol. 2, no. 2, pp. 323–343, 2009.

[35] M. Bertalmio, G. Sapiro, V. Caselles, and C. Ballester, "Image inpainting," in *Proc. 27th Annual Conf. Computer Graphics and Interactive Techniques* (Series SIGGRAPH '00). New York, NY, USA: ACM Press, 2000, pp. 417–424.

[36] V. Caselles, J. Morel, and C. Sbert, "An axiomatic approach to image interpolation," *IEEE Trans. Image Process.*, vol. 7, no. 3, pp. 376–386, Mar. 1998.

[37] D. Ziegler, T. R. Meyer, R. Farnham, C. Brune, A. L. Bertozzi, and P. D. Ashby, "Improved accuracy and speed in scanning probe microscopy by image reconstruction from non-gridded position sensor data," *Nanotechnology*, vol. 24, no. 33, 2013, Art. no. 335703. [Online]. Available: http://stacks.iop.org/0957-4484/24/i=33/a=335703

[38] T. Tuma, J. Lygeros, A. Sebastian, and A. Pantazi, "Optimal scan trajectories for high-speed scanning probe microscopy," in *Proc. 2012 Amer. Control Conf.*, Jun. 2012, pp. 3791–3796.

[39] D. Momotenko, J. C. Byers, K. McKelvey, M. Kang, and P. R. Unwin, "High-speed electrochemical imaging," *ACS Nano*, vol. 9, no. 9, pp. 8942–8952, 2015. [Online]. Available: http://dx.doi.org/10.1021/acsnano.5b02792

[40] B. D. Huey, R. Nath Premnath, S. Lee, and N. A. Polomoff, "High speed SPM applied for direct nanoscale mapping of the influence of defects on ferroelectric switching dynamics," *J. Amer. Ceramic Soc.*, vol. 95, no. 4, pp. 1147–1162, 2012. [Online]. Available: http://dx.doi.org/10.1111/j.1551-2916.2012.05099.x

[41] A. D. L. Humphris, J. K. Hobbs, and M. J. Miles, "Ultrahigh-speed scanning near-field optical microscopy capable of over 100 frames per second," *Appl. Phys. Lett.*, vol. 83, no. 1, pp. 6–8, 2003. [Online]. Available: http://scitation.aip.org/content/aip/journal/apl/83/1/10.1063/1.1590737

[42] J. H. Lee, B. A. Hargreaves, B. S. Hu, and D. G. Nishimura, "Fast 3D imaging using variable-density spiral trajectories with applications to limb perfusion," *Magn. Resonance Med.*, vol. 50, no. 6, pp. 1276–1285, 2003. [Online]. Available: http://dx.doi.org/10.1002/mrm.10644

[43] J.-L. Starck, "Sparse astronomical data analysis," in *Statistical Challenges in Modern Astronomy V* (Series Lecture Notes in Statistics), vol. 902, E. D. Feigelson and G. J. Babu, Eds. New York, NY, USA: Springer-Verlag, 2012, pp. 239–253. [Online]. Available: http://dx.doi.org/10.1007/978-1-4614-3520-4_23

Dominik Ziegler was born in Switzerland, in 1977. He studied at the University of Neuchtel, Neuchtel, Switzerland, and received the M.S. degree in microengineering from École Polytechnique Fdrale de Lausanne, Lausanne, Switzerland, in 2003. After visiting the Biohybrid Systems Laboratory, University of Tokyo, Japan, he received the Ph.D. degree in the Nanotechnology Group, ETH Zurich, Zurich, Switzerland, in 2009.

His research interests include advanced research in micro- and nano-fabrication, bio-MEMS, lab-on-a-chip, and general low-noise scientific instrumentation. His work on scanning probe microscopes focuses on Kelvin probe force microscopy and high-speed applications. As a Postdoctoral Researcher in the Lawrence Berkeley National Laboratory, Berkeley, CA, USA, he developed high-speed techniques using spiral scanning and developed encased cantilevers for more sensitive measurements in liquids. Co-founding Scuba Probe Technologies LLC his work currently focuses on the commercialization of encased cantilevers. Since 2016, he also directs research activities at the Politehnica University of Bucharest, Romania.

Travis R. Meyer received the B.Sc. degree in physics and the B.A. degree in applied mathematics from the University of California, Los Angeles (UCLA), CA, USA, in 2011. He is currently a graduate student working toward the Ph.D. degree in applied mathematics at UCLA.

His interests include variational models for machine learning and data processing, specifically in the domains of signal and text analysis. In addition to his research, he has worked in collaboration with specialists in a variety of domains as well as helped in developing and instructing a machine learning course for the UCLA Mathematics Department.

Andreas Amrein was born in Aarau, Switzerland, in 1989. He received the B.Sc. degree in mechanical engineering and the M.Sc. degree in robotics, systems, and control from the Swiss Federal Institute of Technology, Zurich, Switzerland, in 2013 and 2016, respectively.

From 2014 to 2015, he was with the Lawrence Berkeley National Laboratory. He recently joined Eulitha AG, where he works on photolithographic systems as a Product Development Engineer.

Andrea L. Bertozzi received the B.A., M.A., and Ph.D. degrees in mathematics all from Princeton University, Princeton, NJ, USA, in 1987, 1988, and 1991, respectively.

She was with the faculty of the University of Chicago, Chicago, IL, USA, from 1991 to 1995 and of the Duke University, Durham, NC, USA, from 1995 to 2004. From 1995 to 1996, she was the Maria Goeppert-Mayer Distinguished Scholar at Argonne National Laboratory. Since 2003, she has been with the University of California, Los Angeles, as a Professor of mathematics, and currently serves as the Director of applied mathematics. In 2012, she was appointed the Betsy Wood Knapp Chair for Innovation and Creativity. Her research interests include machine learning, image processing, cooperative control of robotic vehicles, swarming, fluid interfaces, and crime modeling.

Dr. Bertozzi is a Fellow of both the Society for Industrial and Applied Mathematics and the American Mathematical Society; she is a Member of the American Physical Society. She has served as a Plenary/Distinguished Lecturer for both SIAM and AMS and is an Associate Editor for the SIAM journals: *Multiscale Modelling and Simulation*, *Imaging Sciences*, and *Mathematical Analysis*. She also serves on the editorial board of *Interfaces and Free Boundaries*, *Nonlinearity*, *Applied Mathematics Letters*, *Journal of the American Mathematical Society*, *Journal of Nonlinear Science*, *Journal of Statistical Physics*, and *Communications in Mathematical Sciences*. She received the Sloan Foundation Research Fellowship, the Presidential Career Award for Scientists and Engineers, and the SIAM Kovalevsky Prize in 2009.

Paul D. Ashby received the B.Sc. degree in chemistry from Westmont College, Santa Barbara, CA, USA, in 1996 and the Ph.D. degree in physical chemistry from Harvard University, Cambridge, MA, USA, in 2003.

Subsequently, he was part of the founding of the Molecular Foundry, Lawrence Berkeley National Laboratory, Berkeley, CA, USA, as a jump-start Postdoc and transitioned into a Staff Scientist position, in 2007. His research aims to understand the *in situ* properties of soft dynamic materials, such as polymers, biomaterials, and living systems and frequently utilizes scanned probe methods. Recent endeavors include the development of encased cantilevers for gentle imaging in fluid and high-speed AFM scanning. He is a Cofounder of Scuba Probe Technologies LLC.

Queries

Q1. Author: Please check first footnote as set for correctness.